UNESCO - INTERNATIONAL HYDROLOGICAL PROGRAM IV

A methodology for the assessment of surface resistance and soil water storage variability at mesoscale based on remote sensing measurements.

A case study with HAPEX-EFEDA data.

W.G.M. Bastiaanssen**, D.H. Hoekman* en R.A. Roebeling**.

*) Wageningen Agricultural University
Department of Water Resources
**) Winand Staring Centre
Department of Water Management in
Arid Zones

RAPPORT 38 Juli 1993

Vakgroep Waterhuishouding
Nieuwe Kanaal 11, 6709 PA Wageningen

ISSN 0926-230X

The research project was executed on behalf of the International Committee on Atmosphere, Soil and Vegetation Relations of IAHS (ICASVR/IAHS) as a contribution to the IHP-projects H1.1 and H2.1.

At the same time the project is contributing to the IGBP-Core project Biospheric Aspects of the Hydrological Cycle (BAHC) and the World Climate Research Programme.

The report will be also published as Report nr. 2 in the Series Monographs and Reports of the International Association of Hydrological Sciences (IAHS).

Abstract

A new remote sensing algorithm has been tested with Normalized Difference Vegetation Index, surface albedo and surface temperature data obtained during the Thematic Mapper Simulator flight in the HAPEX-EFEDA field experiment (Hydrological and Atmospheric Pilot Experiment-Echival Field Experiment in a Desertification threatened Area). Its high spatial resolution allowed for a comparison of its results with soil moisture obtained from the moisture monitoring network. The microwave backscatter coefficient derived from AIRSAR data provided a possibility to compare the evaporation and topsoil moisture content. Having the surface energy balance instantaneously quantified in a distributed manner, it was finally possible (i) to inversely derive the surface resistance to evaporation from the latent heat flux and (ii) to study the (non-linear) relationship between surface resistance and soil water content at mesoscale for the Mediterranean climate present in Spain.

LIST OF SYMBOLS

Symbol	Interpretation	Dimensions
c_p	specific heat of air at constant pressure	$J.kg^{-1}.K^{-1}$
E_s	actual soil evaporation	$m.s^{-1}$
E_t	actual plant transpiration	$m.s^{-1}$
E	actual evaporation	$m.s^{-1}$
E^*	actual at-surface evaporation	$m.s^{-1}$
e	actual vapour pressure	mbar
e_s	saturated vapour pressure	mbar
G_0	soil heat flux at the land surface	$W.m^{-2}$
H	sensible heat flux	$W.m^{-2}$
$K\downarrow$	incoming shortwave radiation	$W.m^{-2}$
$K\uparrow$	outgoing shortwave radiation	$W.m^{-2}$
K^*	net shortwave radiation	$W.m^{-2}$
k	wave number	m^{-1}
L	surface autocorrelation length	m
L	spectral radiance	$W.m^{-2}.sr^{-1}.\mu m^{-1}$
$L\downarrow$	incoming longwave radiation	$W.m^{-2}$
$L\uparrow$	outgoing longwave radiation	$W.m^{-2}$
L^*	net terrestrial longwave radiation flux	$W.m^{-2}$
$L(\lambda)$	spectral radiance at sensor aperture	$W.m^{-2}.sr^{-1}.\mu m^{-1}$
N	maximum number of sunshine hours	hour
n	actual number of sunshine hours	hour
Q^*	net radiation	$W.m^{-2}$
r_s	surface resistance to vapour transport	$s.m^{-1}$
r_{ah}	aerodynamic resistance to heat transport	$s.m^{-1}$
r_{av}	aerodynamic resistance to vapour transport	$s.m^{-1}$
r_{sh}	soil resistance to heat transport	$s.m^{-1}$
r_{sv}	soil resistance for vapour transport	$s.m^{-1}$
r_p	planetary reflectance	-
$r_p(\lambda)$	spectral planetary reflectance	-
r_0	surface reflectance, surface albedo	-

S	degree of saturation	-
s	r.m.s. surface height variation	m
T_a	air temperature	K
T_s	soil temperature	K
T_0	surface temperature	K
T_0^R	surface radiation temperature	K
T_{sat}	at-satellite radiation temperature	K
T	clear sky transmission factor	-
t	time	s
u	wind speed	$m.s^{-1}$
u_*	friction velocity	$m.s^{-1}$
W	soil water storage	m
v_z	liquid volume flux density	$m.s^{-1}$
z	depth	m
z_e	effective depth of zone of vaporization	m
z_0	aerodynamical roughness length	m
z_{0m}	aerodynamical roughness length for momentum	m
z_{0h}	aerodynamical roughness length for heat	m
z_{0v}	aerodynamical roughness length for vapour	m
γ	psychrometric constant	$mbar.K^{-1}$
ϵ	complex dielectric constant	Farad m^{-1}
ϵ'	apparent emissivity of the atmosphere	-
ϵ_0	surface emissivity	-
θ	soil water content	-
θ_r	residuel soil water content	-
θ_{sat}	saturated soil water content	-
λ	latent heat of vapourization	$J.kg^{-1}$
λ	wavelength	μm
λE	latent heat flux	$W.m^{-2}$
λE_s	latent heat flux from interal soil evaporation	$W.m^{-2}$
λE_0	latent heat flux from at surface evaporation	$W.m^{-2}$
$\rho_a C_p$	air heat capacity	Jm^3K^{-1}
$\rho_s C_s$	soil heat capactity	$Jm^{-3}K^{-1}$
ρ_a	moist air density	$kg.m^{-3}$

ρ_w	water density	$kg.m^{-3}$
ρ_v	vapour densitity or absolute humidity	$kg.m^{-3}$
σ	Stefan Boltzmann constant	$W.m^{-2}.K^{-4}$
σ^0	differential radar cross section	-

CONTENTS

1. INTRODUCTION

1.1 Problem description

Atmospheric Models attempt to simulate the atmospheric motion for daily weather prediction and future global climate change effects (e.g. American Meteorological Society, 1991). The lower boundary conditions in these Atmospheric Models are governed by the heat exchange rates between oceans, land, glaciers and the atmosphere. With respect to heat exchange rates, oceans and glaciers behave spatially rather uniform. Of a more troublesome nature is the spatial heterogeneity of the energy and water balance on land. The spatial dimensions of a grid cell of an Atmospheric Model usually vary between 50 and 1000 km. At such a scale, land consists of different vegetation and soil types including large differences in land wetness and relief. As a direct consequence, the turbulent fluxes of momentum, heat and vapour between land and the lower atmosphere can vary enormously from place to place. Extremely simplified Land Surface Models are conjuncted towards Atmospheric Models to predict the partitioning of the net available energy into sensible- and latent heat fluxes at the mesoscale (among others, Dickinson et al., 1986; Sellers et al., 1986; Noilhan and Planton, 1988). Land Surface Models are denoted to be simple, because (i) water and heat transfer is described as being a solely vertical process only, (ii) the mathematical formulations of the environmental physics is due to availability of input data not complete and (ii) they don't (yet) treat the *natural variability* within a grid cell of an Atmospheric Model. Moreover, techniques to verify the areal mean energy and water balance predicted by Land Surface Models have still to be developed, so that little is known on the reliability of predictions done with current Land Surface Models. Data from earth observation satellites can potentially be better utilized to improve our understanding of the temporal and spatial variability of actual land surface processes. Representative values for the areal energy and water balance of an entire grid cell can be established when at a higher resolution confidence in the estimated heat exchange rates exists. Yet, techniques have to be developed to translate non-homogeneous terrain conditions into areal effective fluxes of momentum, heat and water vapour, allowing a verification of the predictions given by a numerical Land Surface Model.

Factors which govern the land surface hydrological processes and are recognized in a Land Surface Model can be split into several themes:

- *Land state variables* which vary both in time and space, e.g. temperature of vegetation and

soil, soil water content, water vapour densities in vegetation and soil, solar radiation;

- *Land surface parameters* which are quasi-constant with time, e.g. vegetation coverage, surface roughnes, surface albedo, surface emissivity;
- *Top soil properties* which remain constant in time but are distributed within the grid cell, e.g. thermal diffusivity, hydraulic diffusivity and vapour diffusivity.

The resistance to evaporation responds to the topsoil water content, availability of solar radiation, temperature, vegetation coverage and atmospheric humidity (Jarvis, 1976). As such, the resistance to evaporation covers many of the land state variables and surface parameters mentioned above. Remote sensing techniques provide us nowadays with areal spectral data which can help to bridge the gap from local scale to areal mean quantities. Spaceborne scanner systems are under operation in different spectral regions: i.e. the visible, near-infrared, thermal infrared and microwave spectral range. Although remotely operating sensors do not measure the above land features directly, research efforts are currently directed towards making the interpretation from satellite spectral data into some land surface characteristics feasible (e.g. International Satellite Land surface Climatology Project ISLSCP, Becker et al., 1988). Synergetic use of the available spaceborne data is thought to be effective because each spectral information adds value to the spatial inventory of dynamic and constant land surface characteristics.

The present report concerns the determination of the surface fluxes in relation to soil water availability. The study contributes towards the development of an independent tool to verify simulated mesoscale land surface behaviour with numerical Land Surface Models. The reported work is part of the Hydrological and Atmospheric Pilot EXperiment (HAPEX) of the European project on Climate and Hydrological Interactions between Vegetation, Atmosphere and Land surfaces (ECHIVAL), which was executed during the summer of 1991 in Spain (Bolle and Streckenbach, 1992). The Mediterranean climate of Spain was assigned to be a part from the HAPEX study areas (as in France and Niger), because the area belongs to the historic transformation of European climate zones. In the light of desertification-threatened areas, the Meditteranean areas have come again in the publicity. Since space, air and ground truth data were collected simulatenously and scattered over the Castilla la Mancha area (100*100 km^2) by various agencies, the data from this HAPEX experiment was taken as a test out for mutually comparing visible, infrared and microwave data. The feasibility of mapping regional soil moisture and surface resistance variability can be assessed by comparing it with hydro-meteorological field data like the surface fluxes and soil water content.

1.2 Study area

Airborne missions performed during the HAPEX-Spain campaign comprised among others:

- NASA Thematic Mapper Simulator data (TMS-NS001), June 29;
- Joint Propulsion Laboratory, JPL, full polarization synthetic AIRSAR data; C,L, and P band, (calibrated) Stokes representation, June 19 and July 14;

The TMS has flown various lines over the Castilla la Mancha area, out of which the East-West E-F line was chosen as the reference for the present investigation (Fig. 1). Two pilot areas of 15.9*14.4 km^2 each were selected from the original flight strip. The pilot areas were geo-referenced to an UTM coordinate-system. In the upper left corner the Tomelloso pilot area has UTM coordinate x = 496408.5, y = 434441615 while the Barrax pilot area has UTM coordinate x = 568245.2, y = 4333005. The pixel size appeared to be approximately 18.5*18.5 m^2. The acquisition time was 10.19 GMT.

An unsupervised classification of the two regions on the basis of band 3 (blue), 4 (red) and 5 (green) have been performed and is displayed in Figs. 2 and 3. The circular patterns in the Barrax image (Fig. 2) are worth noting. They are all center pivot irrigation systems, which gives them peculiar appearance. The red colours mark a high reflectance in band 4 indicating arable pieces of land. The pink hues appear to be cereals and the vineyards around Tomelloso (Fig. 3) show up as very light green. The dark to black coloured parcels consist of fallow land. Drainage patterns are clearly visible east of Tomelloso, and are due to micro rather than macro relief.

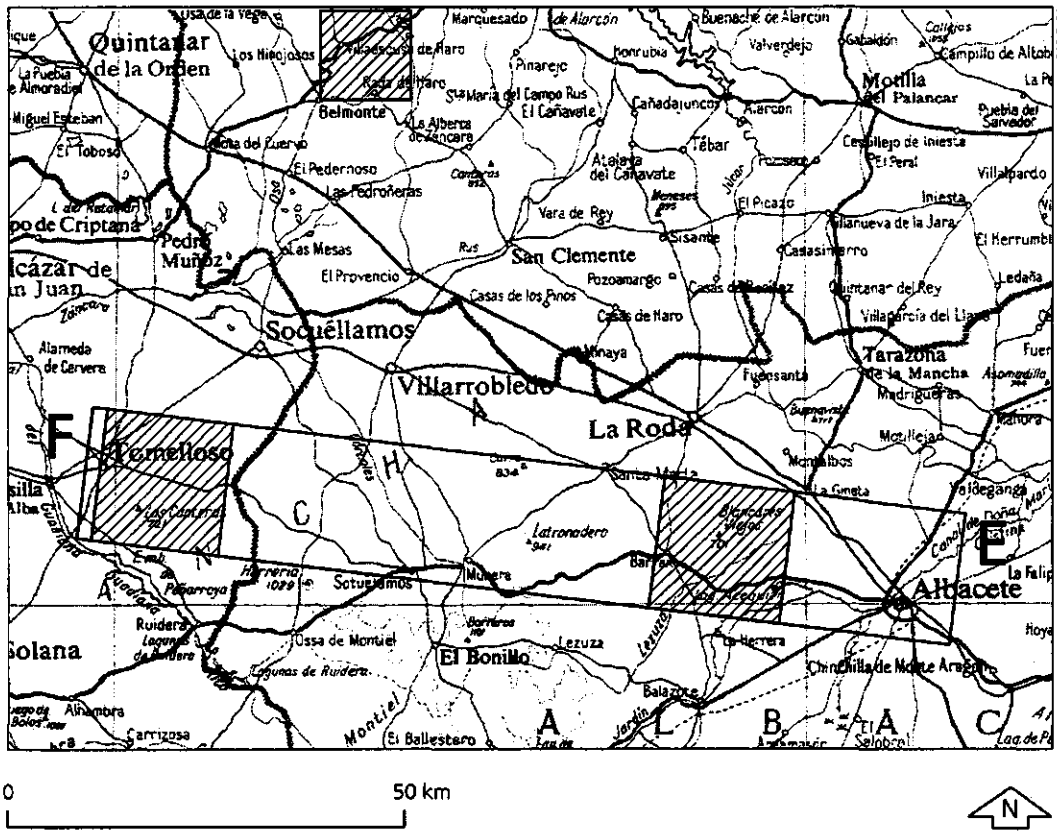

Fig. 1: Location of the study area including the Barrax and Tomelloso areas where intensive ground measurements by the EFEDA team were conducted.

Fig. 2: Colour composite of the Barrax area in Castilla la Mancha, Central Spain. Map is based on Thematic Mapper Simulator band 3 (blue), 4 (red) and 5 (green). Approximate scale 1:85,300

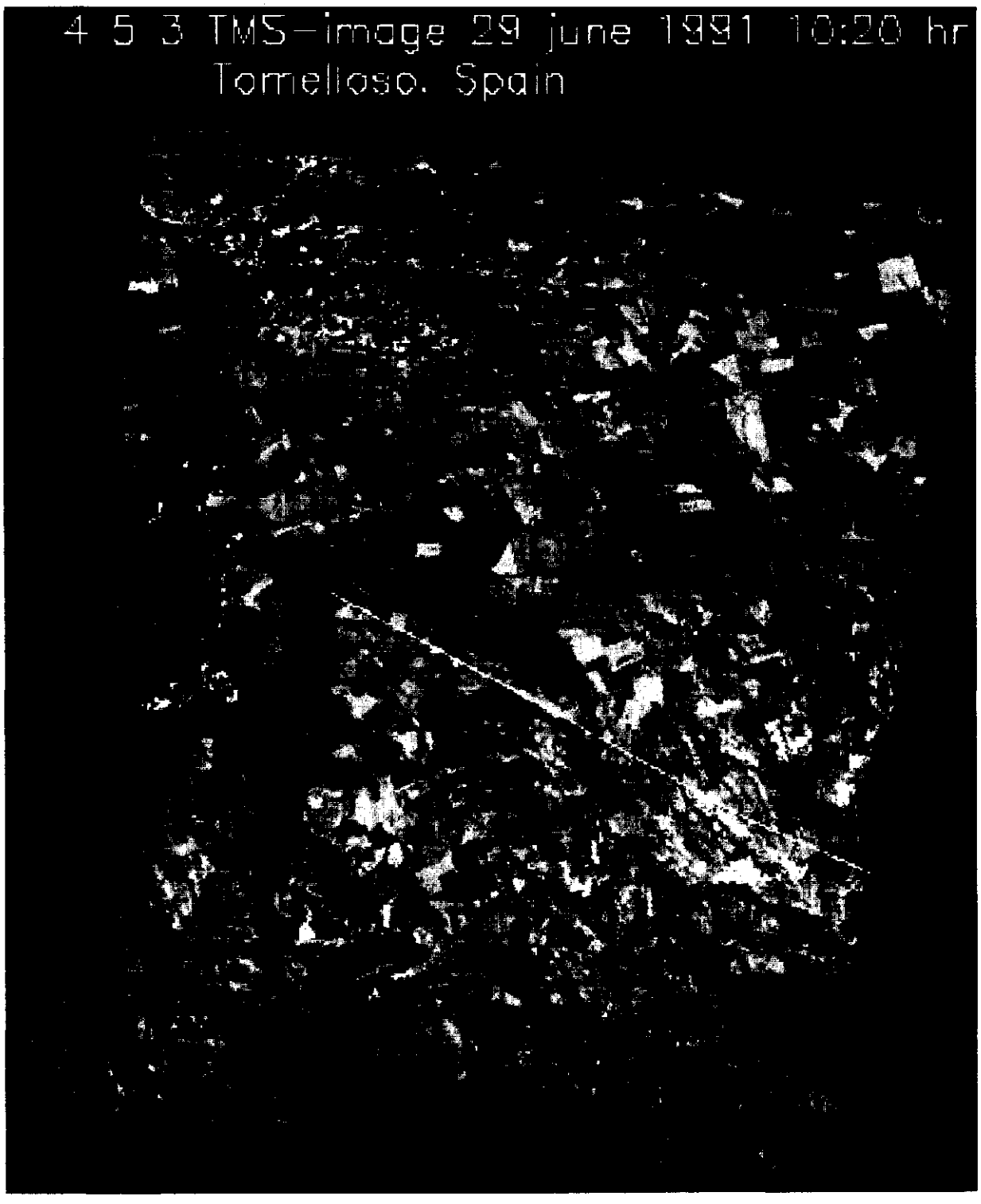

Fig. 3: Colour composite of the Tomelloso area in Castilla la Mancha, Central Spain. Map is based on Thematic Mapper Simulator band 3 (blue), 4 (red) and 5 (green). Approximate scale 1:85,300

1.3 Field investigations

An international group of interdisciplinary agencies took part in a Special Observation Period at Castilla la Mancha during June 1991. The most relevant hydro-meteorological data, collected to support the regionalization of the water and energy balance and analysis of remote sensing images consisted of:

- actual evaporation (eddy correlation and Bowen-ratio system)
- soil heat flux (plate)
- radiation balance (net radiometer, pyranometer)
- surface radiation temperature
- vertical profiles of air temperature
- vertical profiles of soil temperature
- vertical profiles of windspeed
- vertical profiles of atmospheric humidity
- vertical profiles of soil humidity (micro-psychrometers)
- soil moisture (gravimetric and Time Domain Reflectometer)
- soil roughness (needle board)
- surface reflectance (albedo meter)
- spectral measurements in the visible range (handhold spectrometer)

1.4 Study objectives

The objective of the this research is to map out the land surface energy balance pixelwise and determine its associated surface resistance to total evaporation within an acceptable level of accuracy by using a new physically based algorithm (Bastiaanssen, 1993). Spatial temperature and reflectance data (Thematic Mapper Simulator, TMS-NASA) have been used. Soil moisture estimates, using areal values of NASA's JPL-AIRSAR backscatter data were derived for a mesoscale land mosaic. The areas of Tomelloso and Barrax have been seperately analyzed for this purpose. With an adequate spatial description of Normalized Difference Vegetation Index (NDVI), surface abledo (r_o), surface temperature (T_o) and soil water content (θ), it is expected that the following land surface characteristics can be obtained:

- Areal patterns of all surface energy balance components;

- Areal patterns of surface resistance to total evaporation;
- Areal patterns of soil water storage;
- Areal patterns of the thickness of the dry top soil;

Estimates of the actual values of energy balance for a mixed surface coverage type, allows one to calculate the surface resistance to bare soil evaporation in an inverse manner (Bastiaanssen, 1990). Since the surface resistance (which reflects both vegetation and bare soil resistances) is influenced primarily by soil water content, a relationship between the TMS based resistance values and AIRSAR based backscatter coefficients is expected.

The distribution of water content and heat flux densities on the scale of remotely sensed observations can be employed to arrive at areal representative values of the sensible and latent heat flux in relation to their transport resistance and water storage.

2. THEORETICAL ASPECTS OF THE ENERGY AND WATER BALANCE

2.1 Surface energy balance

The energy (and water) balance in semi-arid regions is affected by the presence of fallow- and partially covered dry land and varies therefore strongly from place to place. The energy balance equation can be generally written as:

$$Q^* = H + G_0 + \lambda E^* \qquad (\mathrm{W.m^{-2}}) \qquad [1]$$

where Q^* ($\mathrm{W.m^{-2}}$) is the net radiation (being positive when radiation is adsorbed), H ($\mathrm{W.m^{-2}}$) is the sensible heat flux, G_0 ($\mathrm{W.m^{-2}}$) is the soil heat flux and λE^* ($\mathrm{W.m^{-2}}$) is the latent heat flux (at-surface evaporation). The fluxes of H, G_0 and λE^* are considered positive when directed away from the land surface. Water can flow into the atmosphere, λE, by direct evaporation from the soil, i.e. at-surface evaporation λE_0, sub-surface evaporation λE_s, or through the plant system as canopy evaporation, λE_t:

$$\lambda E = \lambda E_0 + \lambda E_s + \lambda E_t \qquad (\mathrm{W.m^{-2}}) \qquad [2]$$

where λE_0 and λE_t are often combined as λE^* being the at-surface actual evaporation:

$$\lambda E^* = \lambda E_0 + \lambda E_t \qquad (\mathrm{W.m^{-2}}) \qquad [3]$$

Furthermore, the vapour flux density in the lower part of the atmospheric boundary layer, E, can be expressed in full analogue to Ohm's law as a potential difference between the roughness length for vapour tranasport, z_{0v}, and a reference height in the atmosphere, z_a, and an aerodynamic transport resistance, r_{av}, as

$$E = E_0 + E_s + E_t = -\frac{\rho_v(z_{0v}) - \rho_v(z_a)}{r_{av}} \qquad (\mathrm{kg.m^{-2}.s^{-1}}) \qquad [4]$$

The situation for diffusive transfer of water vapour from the wet stomatal cavity of the plants to an external location in the air layer adjacent to the leaf, z_{0v}, reads as (Monteith, 1965):

$$E_t = -\frac{\rho_v^{sat} - \rho_v(z_{0v})}{r_c} \qquad (\text{kg.m}^{-2}.\text{s}^{-1}) \qquad [5]$$

where r_c (s.m^{-1}) is the canopy resistance of the plant. Applying eq. [5] for patches of land implicitly assumes the land to behave like a single 'big-leaf' with saturated vapour inside a type of stomatal cavity. However besides evaporation from canopies, water can also evaporate from the bare soil surface. When the topsoil is bare and dry, the velocity of capillary flow is delayed by molecular forces acting between the soil matrix and water. Mass transport in the dry topsoil then is dominantly established by vapour diffusion, which can be expressed in full analogy to the vapour displacement in air as:

$$E_s = -\frac{\rho_v^{sat}(z_e) - \rho_v(z_0 v)}{r_{sv}} \qquad (\text{kg.m}^{-2}.\text{s}^{-1}) \qquad [6]$$

while at surface evaporation from small water filled capillars reads as

$$E_0 = \rho_w \, v_z \qquad (\text{kg.m}^{-2}.\text{s}^{-1}) \qquad [7]$$

The following meaning is attached to the symbols used in Eqns. (4,5,6,7): r_{av} (s.m^{-1}) is the aerodynamic resistance to vapour transport, r_{sv} (s.m^{-1}) is the soil resistance to vapour transport, r_c (s.m^{-1}) is the canopy resistance, z (m) is the integration or reference height, z_e (m) is the integration depth to obtain r_{sv}, ρ_v (kg.m^{-3}) is the vapour density, ρ_w (kg.m^{-3}) is the water density and v_z (m.s^{-1}) is the capillary rise. To accomplish the various evaporation components sketched, Penman (1948) and later on Monteith (1965) parameterized the lumped actual atmospheric vapour flux density directly (i.e. no mutual substitutions of Eq. (5, 6, 7)) into terms of maximum potential difference and a lumped surface resistance to total evaporation (comprising r_c and r_{sv}), r_s:

$$E = \frac{\rho_v^{sat}(T_0) - \rho_v(z)}{r_{av} + r_s} \qquad (\text{kg.m}^{-2}.\text{s}^{-1}) \qquad [8]$$

This surface resistance to evaporation r_s links energy and water balance modeling since it

functions as the main transport parameter in the latent heat transfer equation and is related to soil moisture availability. In the case of potential canopy evaporation, r_s approaches to a predefined specie dependent minimum value. For open water bodies, r_s can be set to zero (Penman, 1948) while Menenti (1984) came to the same conclusion for bare soil. Likewise the resistance/diffusion formulation of the latent heat transfer by Eq. (8), a transfer heat equation for sensible heat in air, H, and soil G_0, can be formulated by Eq. (9) and (10) respectively :

$$H = -\frac{\rho_a c_p (T_0 - T_a)}{r_{ah}} \quad (\mathrm{W.m^{-}2}) \qquad [9]$$

$$G_0 = \frac{\rho_s c_s (T_0 - T_s)}{r_{sh}} \quad (\mathrm{W.m^{-}2}) \qquad [10]$$

In summary, the land surface energy fluxes can be described by potential differences and the actual values of the transport resistances as follows (Fig. 4):

$\lambda E \rightarrow r_{av}, r_s$

$\lambda E_s \rightarrow r_{sv}$

$\lambda E_t \rightarrow r_c$

$H \rightarrow r_{ah}$

$G_0 \rightarrow r_{sh}$

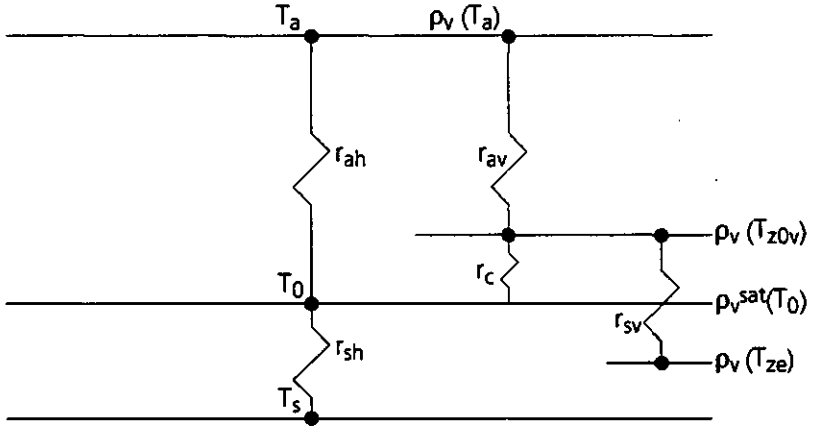

Fig. 4: Representation of the resistances and associated potential differences which regulate the land surface fluxes.

2.2 Soil water balance

Besides the required energy (Q^*), the aerodynamic resistance to vapour transfer (r_{av}) and the drying power of the atmosphere ($\rho_v^{sat}(T_0)-\rho_v(z)$), evaporation is basically controlled by the availability of water. Low evaporation rates (high surface resistance, r_s) go together with a low soil water content, θ, and vice versa. The water storage, W, and evaporation, E, are mutually related through the water balance of a vertical soil column as

$$\Delta W = P + I + Q - E - R - E_i \qquad \text{(m)} \qquad [11]$$

where ΔW is the change in water storage for a given period of time, P the precipitation, E_i the interception, I the irrigation, Q the net upward flow through the bottom of the vertical soil column under consideration and R lateral run-off. The change of water storage with time, $\partial W/\partial t$ over the vertical distance z can more generally be expressed as:

$$\frac{\partial}{\partial z}\left(\frac{\partial W}{\partial t}\right) = \frac{\partial \theta}{\partial t} \qquad (s^{-1}) \qquad [12]$$

where θ (-) is the volumetric soil water content and t (s) is time. If the degree of saturation, expressed as $S=(\theta-\theta_r)/(\theta_{sat}-\theta)$ becomes low, soil water is also present in its vapour phase. Under such conditions, liquid migration is superseded mainly by vapour displacement and depends on:

- degree of saturation of the topsoil;
- the actual water storage in the subsoil;
- drying power of the atmosphere;
- specific permeability of the porous soil system;
- the hydraulic conductivity of the soil to transport water from sub- to topsoil;

The equilibrium between these forces is most commonly found at a typical hooked shape in the soil water content profile, i.e. the so called evaporation front, (Menenti, 1984). Vaporization inside the soil arises when the actual vapour density becomes lower than the saturated vapour density at the ambient temperature. The latent heat required in this process is in this case supplied by the soil heat flux at the evaporation front. Knowledge on the location of the depth of the evaporation front adds information to the interpretation of the remotely observed surface

temperature fields. Namely, if variations of T_0 are observed while the zone of vaporization is rather constant and below the surface, it should be clear that factors, different from the hydrological regime, play a role in the establishment of T_0.

2.3 Brief description of the SEBAL algorithm

From a remote sensing point of view, Eq. (4) cannot be solved since in practice atmospheric sounders cannot (yet) measure $\rho_v(z)$ accurately. Microwave assessements of the topsoil water content are not useful for this purpose since the relation between θ and r_s is not universal. However, the surface energy balance equation can be rewritten and relate λE to the other variables, which are representative for the mixture of land within the pixel of consideration (e.g. Feddes et al., 1993):

$$\lambda E = \underbrace{(1-r_0)K^{\downarrow} + \epsilon' \sigma T_a^4 - \epsilon_0 \sigma T_0^4}_{Q^*} - \underbrace{\rho_a c_p (T_0 - T_a)/r_{ah}}_{H} - \underbrace{\rho_s c_s (T_0 - T_s)/r_{sh}}_{G_0} \quad (\mathrm{W.m^{-2}}) \qquad [13]$$

Conceptually different approaches have been developed to overcome problems associated with estimating λE rates on the basis of remotely-sensed surface temperature in the past. One of the common drawbacks is that the relationship between remotely measured T_0 and λE was often empirically fitted which excludes an application to other (and larger) regions. In large areas, a variety of vertical gradients such as temperatures and humidities differences exists, which are not always in an orderly way related to (near) surface properties such as surface albeo (r_0), roughness length (z_0), soil thermal conductivity (λ'), apparent infrared emissivity of the atmosphere (ϵ') and surface infrared emissivity (ϵ_0). On heterogeneous terrain, properties and state variables usually have an incoherent interrelation, e.g T_a shows no coherence with z_0 for a set of patches. However to make an assessment of the areal patterns of the variables in Eq. (13) feasible, we have chosen for a solution with empirical relationships between the remotely observable entities NDVI, r_0, T_0 and the parameters T_a, z_0, ϵ_0, G_0/Q^*. Towards this end, a new Surface Energy Balance Algorithm for Land, SEBAL was worked out (Fig. 5), which attempts to map out values of r_0, T_0, NDVI, $K^{\downarrow}$, T_a, G_0/Q^*, ϵ', ϵ_0 and z_0 pixelwise which can be substituted in Eq. (13). The surface energy balance can then be solved by subsequently considering Q^*, G_0 and H. Values for λE were obtained as the residue of the surface energy balance (Fig. 5).

Q^* was approximated on a pixel by pixel basis (x,y) with Eq. (14):

$$Q^*(x,y) = K^{\downarrow}(x,y) - r_0 K^{\downarrow}(x,y) + L^{\downarrow} - L^{\uparrow}(x,y) \qquad (W.m^{-2}) \qquad [14]$$

$K^{\downarrow}(x,y)$-values were estimated from the exo-atmosperical radiation as a function of zenith angle and sun-earth distance in combination with a clear sky transmission factor derived from field observations. The (x,y) notation is added to indicate the spatial variability between pixels. Values for r_0 were obtained by plotting the weighted mean planetary reflectances of the six TMS reflectance channels against known r_0-values of specific targets.

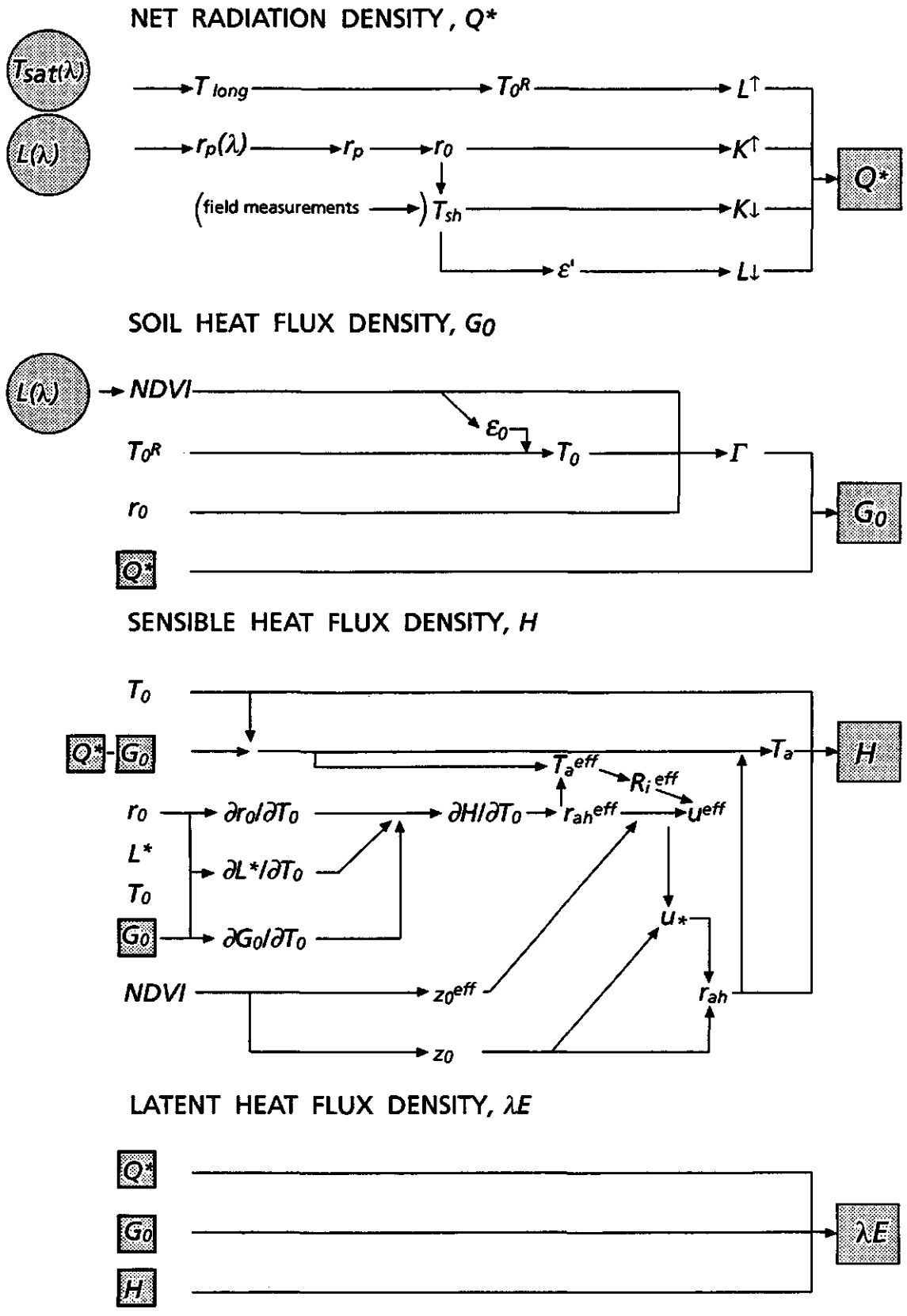

Fig. 5: Four step flow diagram of the Surface Energy Balance Algorithm of Land (SEBAL). Remote data of $T_{sat}(\lambda)$ and $L(\lambda)$ were used as input in addition to scarse ground data.

Values for G_0 were approximated using a G_0/Q^* parameterization of NDVI (to include vegetation effects), r_0 (to include soil wetness and radiation effects) and T_0 (to include energy balance and diurnal variation effects). The fully empirical equation is based on G_0 and Q^* measurements conducted over bare land surfaces at 18 different locations in Egypt. Both winter and summer period observations were included in the regression analysis (Bastiaanssen, 1993). The role of NDVI is added to account for the extinction of solar radiation. So, the T_0, r_0 parameters in Eq. (15) govern the G_0/Q^* ratio for bare soil conditions, whereas NDVI describes the extinction effect when leaves shade the land. At low NDVI values, G_0/Q^* is proportional to $r0'$ and inversely proportional with $T0$ and $r0$. The role of NDVI will become significant when NDVI exceeds say 0.7.

$$G_0/Q^*(x,y) = T_0(x,y)/r_0(x,y)\ (0.32r'_0(x,y) + 0.62r'^2_0(x,y))\ (1 - 0.98\ \mathrm{NDVI}^4(x,y))\ 10^{-2}\ (-) \qquad [15]$$

were T_0 should be explicitly expressed in °C and r_0 and r'_0 are dimensionless. The value of r'_0 represents the average r_0-value for periods when G_0 is directed downward, i.e. during daytime. The combination of $Q^*(x,y)$ and $(G_0/Q^*)(x,y)$ allows the determination of $(Q^*-G_0)(x,y)$. The areal patterns of H were mapped using:

$$H(x,y) = \rho_a c_p \{T_0(x,y) - T_a(x,y)\}/r_{ah}(x,y) \qquad (\mathrm{W.m^{-2}}) \qquad [16]$$

Spatial variation of r_{ah} was accounted on by considering z_0 using the $z_0=f(\mathrm{NDVI})$ functions suggested by Moran (1990) thereby accepting the constraint that the roughness length does not, in all cases, increase with biological activity. The regression coefficients were obtained from the vegetation height and NDVI-values. For Tomelloso, $z_0(x,y)=\exp(-5.5+5.8\ \mathrm{NDVI}(x,y))$ has been used whereas the situation in Barrax is slightly different with $z_0(x,y)=\exp(-5.2+5.3\ \mathrm{NDVI}(x,y))$. The aerodynamic heat transfer coefficient was calculated as:

$$r_{ah}(x,y) = (0.41\ u^*)^{-1} \ln\{z/z_0(x,y)\} \qquad (\mathrm{s.m^{-1}}) \qquad [17]$$

The u_*-value was is in this study considered to be areally constant because the study area was rather flat and tall vegetation was not present. The areal effective u_*-value was derived from $\partial H/\partial T_0$ which on turn was found from $\partial r_0/\partial T_0$, $\partial L^*/\partial T_0$ and $\partial G_0/\partial T_0$ using the approach suggested by Menenti et al. (1989). However, solutions are developed to account on u_* in a spatial manner as well (see Fig. 5). Values for $T_a(x,y)$ could be obtained from the assumed presence of bounds of

the evaporative fraction, $\lambda E/(Q^*-G_0)$. When the evaporative fraction equals one, T_0 and T_a must become approximately similar. The other extreme of the evaporative fraction, being zero, allows to make a second estimate of T_a since in this case $Q^*-G_0=H$ and T_0, r_{ah} are already quanitfied during previous steps. Although the linearity between T_0 and T_a is not yet generally accepted, preliminary fieldwork performed in Egypt and Niger indicate an areal coherence between them allowing to assess $T_a(x,y)=17.3+0.28T_0(x,y)$. Finally, λE could be estimated as:

$$\lambda E(x,y) = Q^*(x,y) - G_0(x,y) - H(x,y) \quad (W.m^{-2}) \qquad [18]$$

In contrast with earlier developed remote sensing algorithms, SEBAL doesn't need ground measurements on T_a (e.g. Moran, 1990) and for surface fluxes like net radiation (e.g. Seguin and Itier, 1983) or numerical water balance-atmosphere models (e.g. Van de Griend et al., 1985 ; Sucksdorff & Ottle, 1990) to compute the land surface evaporation.

3. THE CONTRIBUTIVE ROLE OF REMOTE SENSING IN UNDERSTANDING THE LAND SURFACE HYDROLOGY OF CASTILLA LA MANCHA

3.1 Surface energy balance

3.1.1 Visible and near-infrared spectral information

The presence of vegetation regulates to a wide extent the magnitude of the heat exchange rate of the components of the surface energy balance. For example, the soil heat flux depends very much on the shading effects of the leaves, immediately above. Information on the presence of biomass can be obtained through vegetation indices which are usually based on the characteristic that a low reflectance of plants in the red band (TMS-band 3) coincides with a high reflectance in the near-infrared band (TMS-band 4). This is usually expressed as the NDVI, Normalized Difference Vegetation Index (band4-band3)/(band4+band3). A map of NDVI was compiled for the areas in Barrax and Tomelloso as shown in Appendix 1 and 2. The area around Barrax has a mean NDVI-value of 0.36 (ranging from 0 to 0.77) whereas Tomelloso has a mean NDVI of 0.32 (ranging from 0.23 to 0.58). The wide NDVI dispersion around Barrax can be explained by the center pivot and sometimes sprinkler irrigation systems on risers, while only one single center pivot was encountered in the dominant vineyard area of Tomelloso. As a matter of fact, the NDVI image in combination with precipitation records shows that the soils in Barrax must be artificially supplied with water. Yet the average vegetation coverage for both agricultural study areas is the same but with significant more spatial variation in Barrax. Consequently, the variation in energy- and water balance from this view point might expected to be much more dispersed in Barrax. Furthermore, the land surface at Barrax is rougher in the aerodynamic sense, which facilitates the heat and vapour release into the atmosphere.

The net amount of energy reaching a surface is to a large extent regulated by the surface hemispherical reflectance, or so called surface albedo, r_0. Vegetated surfaces usually have a relative low value of albedo, i.e. between r_0= 0.15-0.25, because a lot of solar radiation is absorbed by the chlorophyll in the leaves. The study areas typically show values in the range between 0.20-0.40, and even higher, because the mineralogy of bare soils and surface roughness contribute to the reflectance behaviour as well. Wet soil considerable decrease the reflectance such as after an irrigation turn. The surface albedo can be determined utilizing all visible and infrared spectral data, rather than band 3 and 4 only. The planetary albedo has been extracted from the

TMS data applying a weighing procedure for bands 2,3,5,7,9 and 10. A linear regression according $r_p(x,y)=0.058+0.68\ r_0(x,y)$ appeared to be accpetable ($R^2=0.96$) (see Fig. 6). It appeared afterwards that the atmospheric correction procedure suggested by Koepke et al. (1985) could be used to estimate r_0 from r_p when no ground data are available (as in almost every region).

The mean $<r_0>$ at the moment of acquisition was for Barrax and Tomelloso with respectively 0.22 and 0.23 nearly identical. The range at Barrax ($r_{0min}=0.09$ and $r_{0max}=0.38$) is slightly higher than at Tomelloso ($r_{0min}=0.11$ and $r_{0max}=0.37$). The frequency distributions of the two areas are however completely different. At Barrax, clearly the irrigated and non-irrigated patches can be discriminated, while for Tomelloso only a single class of the partially vegetated vineyards exist. Maps with the r_0-values are given in Appendix 3 and 4.

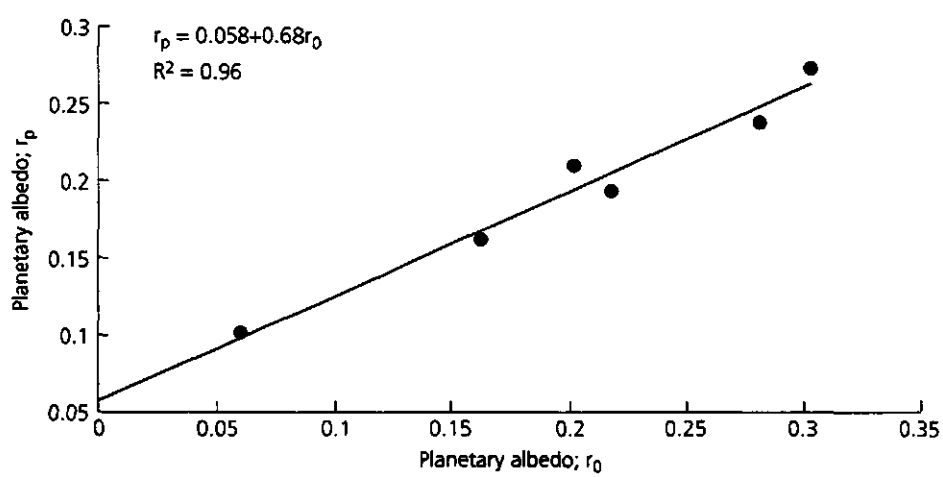

Fig. 6: Regression analysis between planetary albedo derived from at-Thematic Mapper Simulator measured spectral reflectance data and at-ground measured surface albedo ($R^2=0.96$).

3.1.2 Thermal infrared spectral information

Thermal infrared data can be employed to estimate the status of the partitioning of net radiation into the turbulent heat fluxes and the soil heat flux. Surface temperature reveals the equilibrium state condition between all the flux terms. Surface temperature is a key parameter which induces

heat transfer both in the fast atmosphere system, H, and the slow soil system, G_0. Mapping of areal T_0-patterns in combination with an indication of the net heat absorption from the r_0-value, certainly increases the insight of the hydrological status at the land surface. Many publications underline the utility of T_0 measurements to monitor λE (e.g. Choudhury, 1989; Schmugge and Becker, 1991; Engman and Gurney, 1991).

$L^{\uparrow}(x,y)$ in Eq. (14) was quantified according the $T_0^R(x,y)$-values obtained from the thermal infrared channel using Stephan Boltzmann's law. A crude correction procedure with surface measured $L^{\uparrow}(x,y)$-values was invoked to adapt the at-satellite measured $L^{\uparrow}(x,y)$-values for atmospheric heat absorption and emission. The empirical relationship between NDVI and ϵ_0 developed by van de Griend and Owe (1992) for a savanna environment in Botswana has been applied to convert $L^{\uparrow}$ into T_0. Measurements of NDVI and ϵ_0 were made at the site in Tomelosso, confirming (Owe, 1992) that the empirical character of the Botswanian regressions also holds for the vineyards at Tomelloso. The equation reads as

$$\epsilon_0(x,y) = 1.009 + 0.047 \ln \mathrm{NDVI}(x,y) \quad (-) \qquad [19]$$

Subsequently, T_0-values for each pixel could be reconstructed considering a constant relative atmospheric heat absorption and a variable ϵ_0. The mean T_0 at Tomelloso was 44.1 °C while the mean values at Barrax of T_0=33.3 °C was considerably lower. At first glance, these results are unexpected, because the mean r_0 and NDVI values for the two study areas are not very different. Looking more carefully to the theoretical aspects of T_0, we came to the conclusion that factors different from hydrological ones such as turbulence, surface roughness, soil thermal properties and the shape of the $z(\theta)$ profile may play an important role as well. The range of ΔT_0 across the image was found to be respectively 30 °C and 20 °C for Tomelosso and Barrax. Appendix 5 and 6 show the T_0 patterns on June 29, 1991.

3.1.3 Qualitative description of mesoscale exchange processes

Barrax, irrigated agriculture

Interrelating NDVI, r_0 and T_0 shows whether the functioning of the actual land surface process agree with the theoretical and mathematical models of our environment as outlined in Chapter 2. Plotting NDVI vs T_0 for Barrax exibits a good correlationship among them (Fig. 7A) (R^2=0.86).

The data points could be fitted with T_0 = 319.5-34.5 NDVI. The irrigated and non-irrigated classes of land go over the other cluster, revealing a kind of areal linear 'water-biomass-evaporation-temperature' system. When water and biomass are present indeed, the surface resistance, r_s (stomata behaviour) regulates the cooling and heating of the leaf (or at pixel scale it cools or heats the land surface). Since the land surface is not entirely bare, the scatter of the NDVI-T_0 values in the high temperature range is still acceptable low. Realize that at bare land, T_0 is not anymore related to NDVI.

Fig. 7B reveals the presence of an 'evaporation controlled' land surface system having a low albedo in combination with a low surface temperature. The irrigated areas can be found in the zone where the slope between r_0 and T_0 is positive, revealing that with moist land, the surface remains cool, while the temperature reaches its maximum around r_0=0.27. A previous remote sensing study conducted in Egypt, using a Thematic Mapper image with an area of 100*100 km^2, shows also that the maximum T_0 arises at $r_0 \sim 0.27$ (Bastiaanssen, 1990). The value for T_0 will start to decrease if r_0 further increases, yielding a negative slope between r_0 and T_0. The latter category of land can be found back in the righthand ellipse of Fig 7B which occur to be situated at the eastern part of the Barrax image (see Appendix 3).

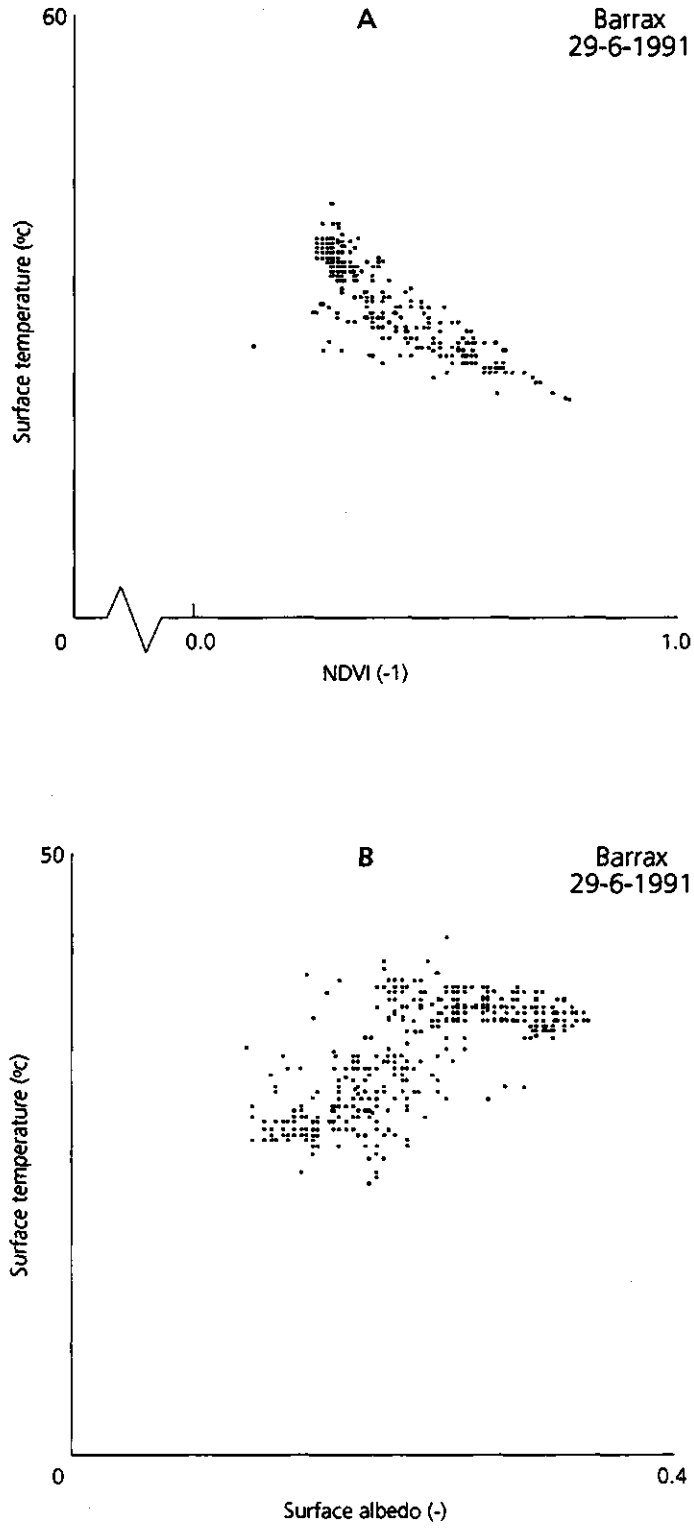

Fig. 7: Scattergrams between Normalized Difference Vegetation Index, surface albedo and surface physical temperature for a 125 km^2 area around Barrax in Castilla la Mancha, Central Spain; Fig. 7A NDVI vs temperature; Fig. 7B albedo vs temperature.

Tomelloso, dry land agriculture

The extensive agricultural patterns around the town of Tomelloso, induces a less coherent structure between NDVI and T_0 (R^2=0.17) then was observed at Barrax (Fig. 8). As explained, the frequency distribution of NDVI consists of a very small range. Since areas with a NDVI higher than 0.5 are rarely found, temperatures lower than 35 °C will not show up frequently. In fact Tomelloso might be conceived as a single land surface hydrology cluster while Barrax clearly contain three or more separated hydrologically identical classes.

It is worth noting as stated before that T_0 is not only modulated by NDVI and r_0, because pixels with the same r_0 and NDVI don't necessarily have the same T_0-value. The group of pixels at Tomelloso with NDVI=0.3 shows to have a temperature of T_0=40 °C while at Barrax the same NDVI=0.3 agrees with T_0=30 °C. Besides difference in soil and crop characteristics, differences in soil water content and wind field might explain the systematic discrepancies noted. The scattergram between T_0 and r_0 can be applied to study the aerodynamic situation above dry land. Towards this end the 'radiation controlled' branche with a negative slope between T_0 and r_0 at Tomelloso shows a more steep pattern than the one at Barrax. The variation of surface temperature, ΔT_0, at a fixed increment of Δr_0 between r_0=0.30-0.40 is larger in Tomelloso because the windspeed is lower than observed at Barrax. At a lower windspeed and a preserved sensible heat flux, the surface to air temperature difference will become larger, which results in higher T_0-values. The slope of the $T_0(r_0)$ relationship can be analytically related to the aerodynamic resistance to heat transfer without having further ground data available according a procedure raised by Menenti et al. (1989) and Bastiaanssen (1990).

Furthermore, it appears that Tomelloso doesn't contain an 'evaporation controlled' surface temperature. Except the one and only irrigation system present in the Northeastern part of the Tomelloso image (see Fig. 3), surface temperature is simply set by the radiation budget, rather than by the hydrological regime. It might be concluded that the T_0-r_0 diagrams can be used to infer main classes with different land surface hydro-meteorological processes, because they provide more information on the actual situation than the NDVI-T_0 relationship gave.

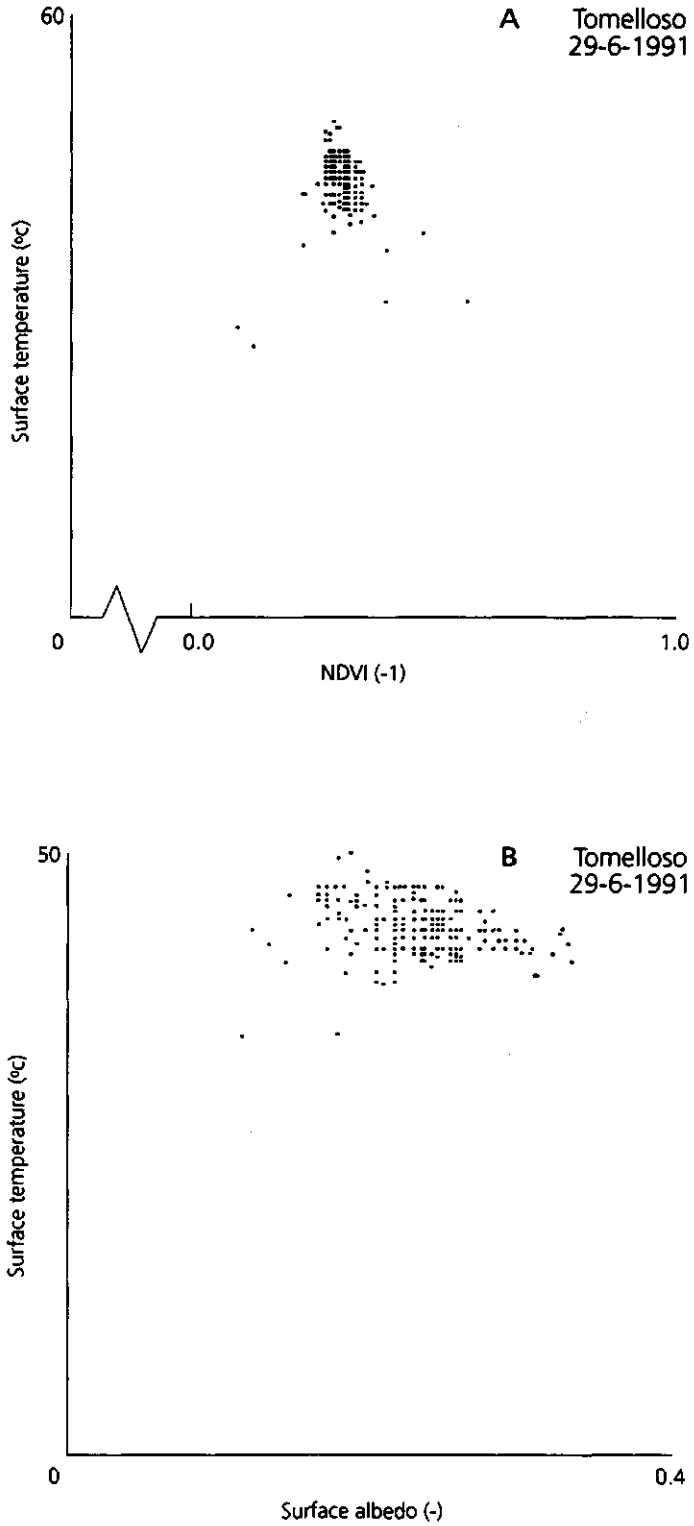

Fig. 8: Scattergrams between Normalized Difference Vegetation Index NDVI, surface albedo and surface physical temperature for a 125 km^2 area around Tomelloso in Castilla la Mancha, Central Spain; Fig. 8A NDVI vs temperature; Fig. 8B albedo vs temperature.

3.1.4 Estimation of the pixelwise land surface fluxes

A quantitative analysis of the surface fluxes can be made after exposing the NDVI-r_0-T_0 data array to the calculation scheme presented in Fig. 5. The frequency distributions of all surface energy balance terms were compiled on the basis of 862*777 pixels for both pilot areas (Figs. 9 and 10). The information given in brackets indicates which parameters are treated variable at the highest scale resolution, i.e. a pixel.

- net radiation, Q^* (variable: r_0, T_0, $K^{\downarrow}$, ϵ_0)
- soil heat flux, G_0 (variable: r_0, T_0 and NDVI in the G_0/Q^* ratio)
- sensible heat flux, H (variable: T_0, T_a, r_{ah})
- latent heat flux, λE ($\lambda E = Q^*-G_0-H$)

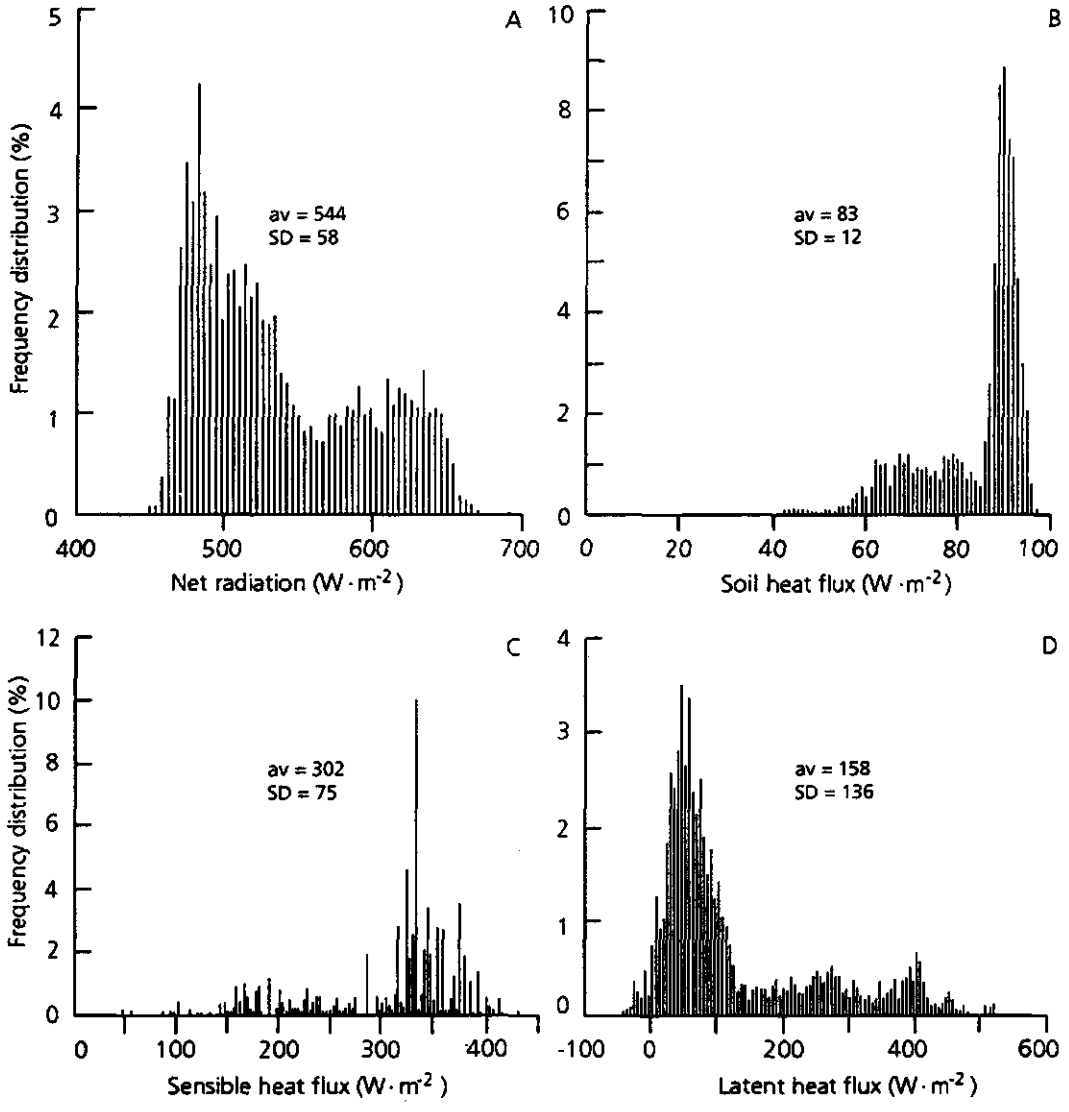

Fig. 9: Frequency distributions of the complete land surface energy balance for the Barrax pilot area, based on 862 * 777 pixels with a size of 18.5*18.5 m² each.

a. Net radiation (Q^*)

b. Soil heat flux density (G_0)

c. Sensible heat flux density (H)

d. Latent heat flux density (λE)

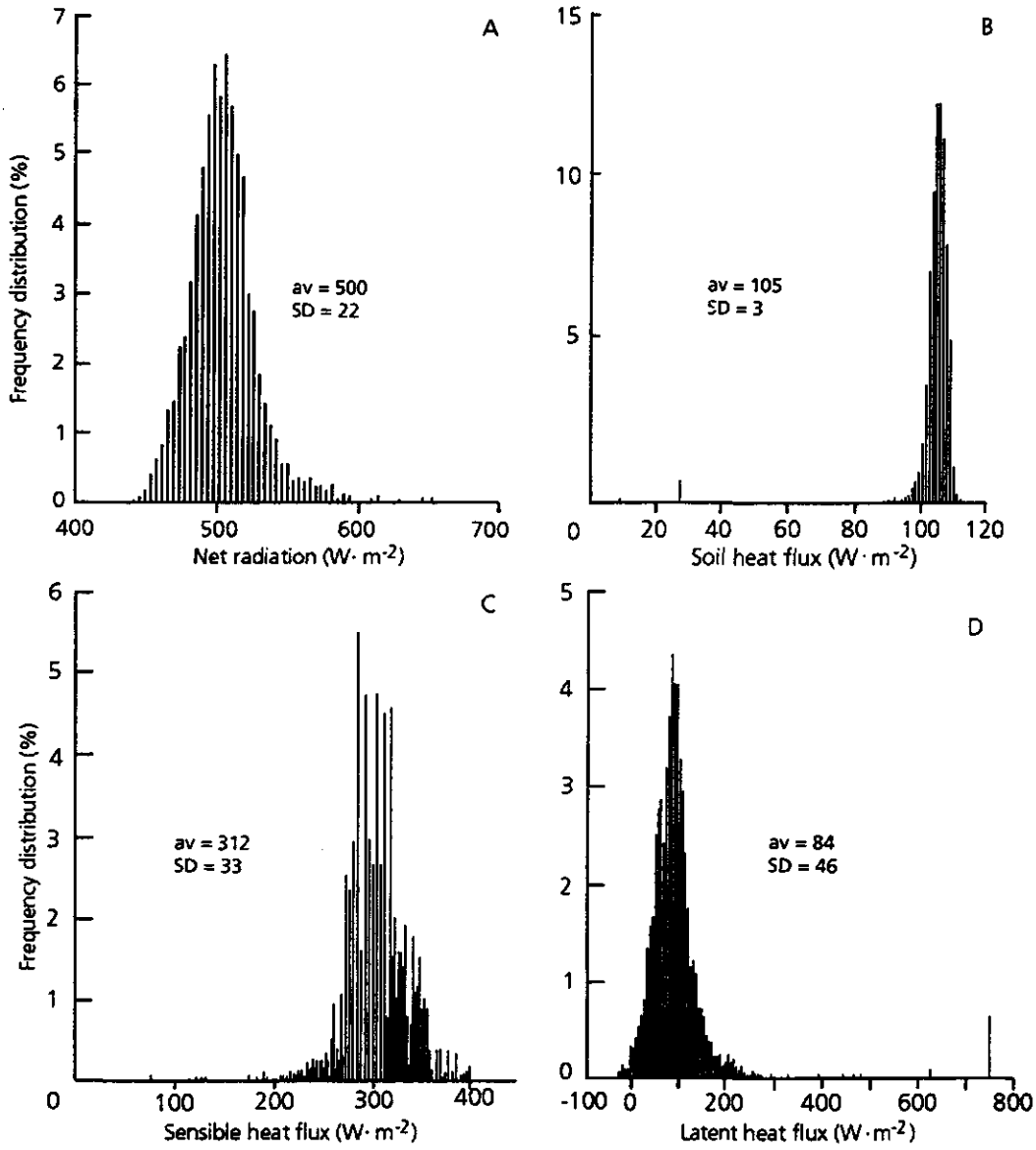

Fig. 10: Frequency distributions of the complete land surface energy balance for the Tomelloso pilot area, based on 862 * 777 pixels with a size of 18.5*18.5 m^2 each.

a. Net radiation (Q^*)

b. Soil heat flux density (G_0)

c. Sensible heat flux density (H)

d. Latent heat flux density (λE)

Barrax, irrigated agriculture

The Barrax pilot area consists of 35 % of irrigated land. The Q^*-patterns of Barrax had a wide diversity (Fig. 9a: $<Q^*>$ = 544 W.m^{-2}; SD = 58 W.m^{-2}). The chevron brackets indicate that it concerns an areal average value. The peak in $Q^*(x,y)$ occurrence (4.4% of pixels having Q^* = 480 W.m^{-2}) was close to $<Q^*>$ = 500 W.m^{-2} of Tomelloso. These pixels represent the traditionally cultivated areas, having a higher albedo (r_0 = 0.28) than the dry farmed soils of Tomelloso (r_0 = 0.23). The latter can be explained most probably by the lower concentration of iron conglomerates present in Barrax. The atmosphere was treated as being vertical and lateral homogeneous, allowing to hold $L^\downarrow$ = 470 W.m^{-2} constant for the pilot area valid for the TMS overpass. The clear sky transmission factor derived from field observations was fixed at 66 %. The artificially irrigated areas showed up by higher $Q^*(x,y)$-values due to lower $r_0(x,y)$ and $T_0(x,y)$-values. The remarkable high Q^*-range (450-670 W.m^{-2}) reveals a wide diversity of the land hydrological conditions. As a direct consequence, G_0 varied considerably as well (Fig. 9b: $<G_0>$ = 83 W.m^{-2}; SD = 12 W.m^{-2}) where the lower G_0-values represent the areas with a high leaf area index and the higher G_0-values the non-irrigated parts (and consequently higher T_0). The overall G_0/Q^* ratio for Barrax was 15%. The dispersion of the H-values was larger as compared to Tomelloso (Fig. 9c: $<H>$ = 302 W.m^{-2}; SD = 75 W.m^{-2}). The typical peaks of sensible heat (percentage of pixels > 4%) traced in the Tomelloso area, also appeared in the Barrax area. The higher windspeed at Barrax further enhanced the T_a-difference between the two agricultural regions. The distribution of λE below 180 W.m^{-2} looks similar to the curve of Tomelloso, revealing that the evaporation rates from dry land in the EFEDA grid cell were all rather similar. A large group of pixels also contributed to λE above 180 W.m^{-2} (Fig. 9d). Consequently the overall evaporation was significantly higher ($<\lambda E>$ = 158 W.m^{-2}; SD = 136 W.m^{-2}) than the analysis of λE in Tomelloso showed. The maximum value of λE = 530 W.m^{-2} was lower than the maximum λE-value observed in Tomelloso.

Tomelloso, dry land agriculture

The Q^*-values appeared to be normally distributed (Fig. 10a). With $<r_0>$ = 0.23 and $<K^\downarrow>$ = 740 W.m^{-2}, $<Q^*>$ becomes 500 W.m^{-2} (SD = 22 W.m^{-2}), which means that L^* equals to -70 W.m^{-2}. Between the western boundary of the Tomelloso-pilot area and the eastern boundary of the Barrax-pilot area there was a difference of only $\Delta K^\downarrow(x,y)$ = 6 W.m^{-2}. The $G_0(x,y)$-values were marked by a small spatial range (SD = 3 W.m^{-2}), because the vegetation was rather even over

this dry farming area. The mean value was $<G_0>$ = 105 W.m^{-2} (Fig. 10b), so G_0/Q^* approached 21%. This is an acceptable value for sparsely vegetated land. The H(x,y)-values differed considerably across the area (Fig. 10c: $<H>$ = 312 W.m^{-2}; SD = 33 W.m^{-2}). It should be noted that spots with a high $T_0(x,y)$-value in combination with a high $z_0(x,y)$-value, such as low transpiring cereals, make significantly contribution in the total flux of H. The u_*-value was 0.39 m.s^{-1}. The $\lambda E(x,y)$-values showed a normal distribution which can be characterized by $<\lambda E>$ = 84 W.m^{-2} with SD = 46 W.m^{-2} (Fig. 10d). The relative low λE-value was established after the dominantly present vineyards with a low soil cover percentage (30 %). The precipitation records of June 1992 in Tomelloso showed a monthly value of less than 10 mm which explains the low bare soil evaporation rate.

3.1.5 Mapping of the surface resistance variability at mesoscale

The surface resistance to evaporation can be determined pixelwise from the $\lambda E(x,y)$, $T_0(x,y)$, $T_a(x,y)$ and $r_{ah}(x,y)$ data array. One underlying assumption is that r_{ah} is similar to r_{av} and that the screen height relative humidity at 10 meter height does not change over the area. The similarity between r_{ah} and r_{av} depends basically on the roughness lengths for atmospheric heat and vapour transport. The source heights where heat and vapour arise are however unpredictable for sparse canopies on a regional scale. For instance in a pivot scheme, sensible heat arises both from bare soil (low roughness) and crops having water deficit (high roughness). The actual vapour density at screen height is a function of T_a and RH. Since no function on the variation of the atmospheric humidity data is available, we simply took the relative humidity value measured at a single point in Tomelloso, being 40 % during acquisition. Then Eq. (8) can be re-written in terms of r_s:

$$r_s = \frac{\rho_v^{sat}(T_0) - \rho_v(z)}{E} - r_{av} \qquad (\text{s.m}^{-}1) \qquad [20]$$

Taking the λE-T_0-T_a-$r_{ah}(x,y)$ array and Eq. (20), it became finally feasible to generate a map of r_s (Appendix 7 and 8). The maximum value of r_s was a-priori set at 900 and 2400 s.m^{-1} for respectively Barrax and Tomelloso. The low resistance show up at land with sprinkler systems (r_s= 20 s.m^{-1}). Appendix 7 show that the resistance of cropped pivots lies between 20-150 s.m^{-1} (average r_s= 50 s.m^{-1}). The traditional rainfed agricultural zones, representing a lion's part of the

area, have a strongly reduced evaporation at this mid-summer image with r_s ranging from 600-2400 s.m^{-1}. Fig. 11 shows the frequency distribution of the evaporation conductance, r_s^{-1}. Conductance is preferred above resistances to ignore the problem of comprising assymptotically large r_s-values in a distribution function. Inspection of Fig. 11 reveals that the Tomelloso curve looks to behave as a gamma-distribution function, which was for mathematical reasons also suggested by Dolman (1992). The median in this case was 0.002 m.s^{-1} being equivalent to r_s=500 s.m^{-1}. However, the shape of the probability density function to describe the spatial variation of r_s^{-1} in Barrax is much more difficult to statistically express.

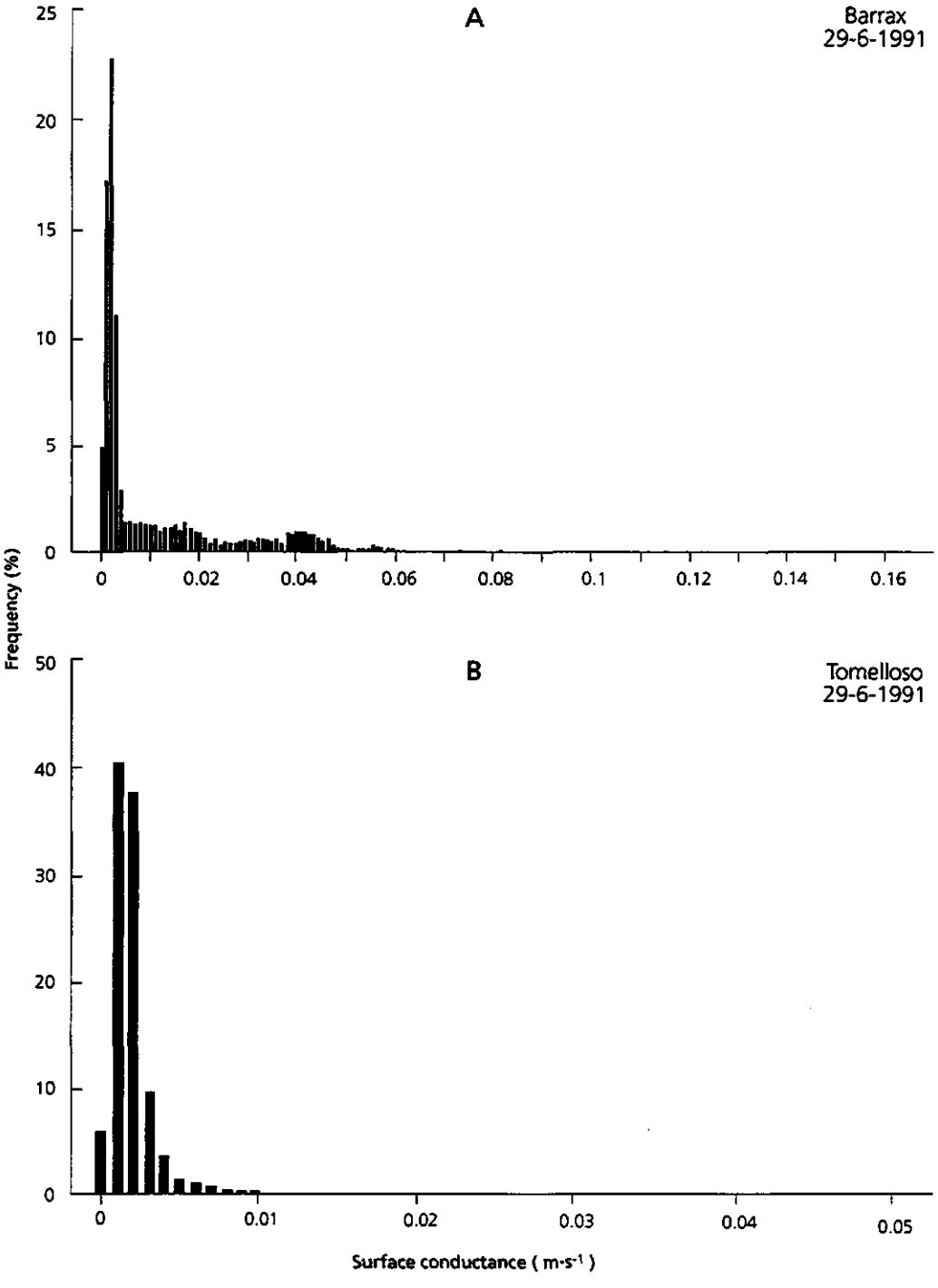

Fig. 11: Frequency distribution of the surface conductances to evaporation for the Barrax area (A) and Tomelloso area (B), based on 862*777 pixels with a size of 18.5*18.5 m^2 each.

3.2 Soil water storage

3.2.1 General

Conventional point measurements are not suitable to describe the spatial variation of soil water content, over length scales of 50 km and more. Remote sensing data has potential for providing areal values rather than point values. For this reason, the application of passive and/or active microwave systems may improve the quantification of areal moisture distribution at the land surface significantly. Methods to estimate soil moisture by means of microwave radiometry developed so far, have a very limited applicability and, particularly, require a-priori knowledge of soil type and hydrological situations. The application of active microwave techniques including different bands (C, L, P) allows for information on the variation of soil moisture with depth, because the penetration depth of these bands is usually frequency dependent. Modeling of the interaction mechanisms (Ulaby and Elachi, 1990; Kong 1990) in combination with an experimental approach using the JPL SAR, should indicate the feasibility of the determination of soil moisture and depth of the evaporation front. Multi-frequency radar (C, L and P band) might be suitable to map out the hooked shape of the soil water content profile present at the depth of the evaporation front. The C-band is useful in the determination of the moisture content of the upper part of the dry toplayer encountered in Spain, whereas the L and P band might be useful in determining the moisture content of the toplayer as a whole.

For practical applications scattering of electromagnetic waves by rough surfaces can be described by three types of relatively simple models (Ulaby et al., 1982). These models are the small perturbation model, the physical optics model and the geometrical optics model. More elaborate models have been applied to derive validity ranges for these simple models (Tsang et al., 1985). When using polarimetric data the HH/VV polarization ratio, can be applied to determine soil moisture in a more direct way, independently of an exact knowledge of surface roughness (Shi et al., 1991). A simple algorithm then follows that can be applied for bare soil pixels. Bare soil pixels can be recognized more or less by its polarimetric scattering behaviour (van Zijl, 1989).

Because of the large length of P-band waves (68 cm) and the relatively dry conditions of the toplayer, waves are expected to penetrate deep, reaching the evaporation front without strong attenuation losses. The evaporation front, which can be seen as a sharp boundary between two layers with very different permitivities, is expected to cause strong reflections which can be detected by the radar. New and relevant application of modern radar systems, such as soil moisture determinations in deeper soil layers (P-band) or the assessment of vertical soil water

content classes is expected to become valuable when microwave soil interactions are properly described and quantified.

3.2.2 Theory of rough surface wave scattering

Fresnel reflection

Wave scattering at a (horizontal) *plane* interface between two homogeneous (non-magnetic) dielectric media can be described by the Fresnel reflection and transmission coefficients, Snell's law and the dielectric properties of the upper and lower medium.

With

$$R_{hh}(\theta_i) = \frac{\cos\theta_i - \sqrt{\varepsilon_r - \sin^2\theta_i}}{\cos\theta_i + \sqrt{\varepsilon_r - \sin^2\theta_i}} \qquad [21]$$

and

$$R_{vv}(\theta_i) = \frac{\varepsilon_r \cos\theta_i - \sqrt{\varepsilon_r - \sin^2\theta_i}}{\varepsilon_r \cos\theta_i + \sqrt{\varepsilon_r - \sin^2\theta_i}}, \qquad [22]$$

as the Fresnel reflection coefficients for horizontally and vertically polarized plane waves, respectively, where θ_i is the angle of the incident wave and ε_r is the ratio $\varepsilon_2/\varepsilon_1$ of the complex dielectric constants of the lower and upper medium. The vertical and horizontal components of the incident and scattered electric field vector $\boldsymbol{E}$ are related as:

$$\begin{pmatrix} E_h^s \\ E_v^s \end{pmatrix} = \begin{pmatrix} R_{hh} & 0 \\ 0 & R_{vv} \end{pmatrix} \begin{pmatrix} E_h^i \\ E_v^i \end{pmatrix} \qquad [23]$$

For scattering at the air/soil boundary ε_r can be assumed to equal the relative complex dielectric constant of the soil layer (ε_2), because the relative dielectric constant of air (ε_1) is very close to unity. The propagation of the scattered wave is in specular direction (at an angle $-\theta_i$).

If the power of an incident wave with polarization p is $I_{0,p}$, then a fraction $\Gamma_{pp} = |R_{pp}|^2$ of the power is reflected in specular direction and a fraction $T_{pp} = 1 - \Gamma_{pp}$ is transmitted through the surface boundary. Γ_{pp} and T_{pp} are called the reflectivity and transmissivity, respectively. The propagation direction θ_r of the refracted wave follows from Snell's law of refraction:

$$\sqrt{\varepsilon_2}\ \sin\theta_r = \sqrt{\varepsilon_1}\ \sin\theta_i \qquad [24]$$

Sub-surface wave propagation

In a homogeneous medium the power of the refracted wave decreases exponentionally, depending on wavelength and dielectric constant. A penetration length can be defined as the length L_p at which the power has decreased to a factor 1/e of the refracted power at the surface boundary (i.e. of $T_{pp}\, I_{0,p}$). L_p is given as:

$$L_p = \frac{\lambda}{4\pi}\ \frac{1}{\sqrt{|\varepsilon_r|}\ \sin\ ½\delta}\ , \qquad [25]$$

where δ is the so-called tangent loss angle ($\tan\delta = \mathrm{Im}(\varepsilon_r)/\mathrm{Re}(\varepsilon_r)$), and λ is the wavelength in free space. Inside the medium the wavelength decreases to $\lambda/\sqrt{|\varepsilon_r|}$.

Description of surface roughness

A rough surface is usually described in terms of its deviation from a plane 'reference' surface. For soil surfaces the roughness often is a result of random processes. The statistical properties of such a random rough surface can be characterized mathematically by measures such as height probability distribution, surface correlation length or power spectral density function.

Soil roughness measurements of agricultural fields can be carried out with a needle board, yielding precise measurement of the surface height profile $h(.)$ over a certain sample length. The profile can be measured in the direction of cultivation determined by plant rows and soil surface ridges $h(x)$ and perpendicular to that direction $h(y)$. Under the assumption that the physical processes that cause surface roughness are uncorrelated for the x- and y-directions, measurements restricted to these two directions are sufficient.

Estimations of r.m.s. height or σ can be determined directly from samples of $h(x)$ and) $h(y)$, yielding σ_x and σ_y. Also estimations of the autocorrelation funtions $C(x)$ and $C(y)$, in x- and y-directions respectively, follow. Because of the assumed independance between the two directions $C(r) = C(x).C(y)$. The autocorrelation lengths l_x and l_y are defined as the distance at which the normalized autocorrelation functions (for which $C(0) = 1$) fall off to a value of 1/e.

The power spectral density (PSD) function is usually defined as the Fourier transform of the un-normalized autocorrelation function:

$$W(\bar{k}) = \frac{\sigma^2}{(2\pi)^2} \int_{-\infty}^{\infty} C(r)\, e^{i\bar{k}r}\, dr \qquad [26]$$

and is also called the surface roughness spectrum. Here $\bar{k}$ is the spatial wave number of the surface ($k=2\pi/\lambda$), which in this case is related to the electromagnetic wave number k by the expression

$$\bar{k} = 2k \sin\theta_i \qquad [27]$$

Also from the PSD function the autocorrelation lengths l_x and l_y can be derived from the points where the normalized PSD function falls off to the value 1/e as $l_{xy} = 2\pi/k_{xy}$. Using the theorems of Wiener-Khintchine and Parseval it can easily be shown that the total area under the power spectrum gives the variance, or 'power' of the surface:

$$\int_{-\infty}^{\infty} W(\bar{k})\, d\bar{k} = \sigma^2 . \qquad [28]$$

The theory of wave scattering from rough surfaces often assumes that surface autocorrelation functions are Gaussian and may be given as

$$C(r) = \exp(-r^2/l^2)$$

Then, the surface roughness spectrum $W(\bar{k})$ follows as

$$W(\bar{k}) = \frac{\sigma^2 l^2}{4\pi} \exp\left(\frac{-\bar{k}^2 l^2}{4}\right) \qquad [29]$$

or, in the direction of wave propagation,

$$W(2k \sin\theta_i, 0) = \frac{\sigma^2 l^2}{4\pi} \exp(-k^2 l^2 \sin^2\theta_i) \qquad [30]$$

Backscattering from random rough surfaces

At a plane surface the wave is scattered in the specular direction. This means that backscattering only occurs when the incident wave is at normal direction (θ_i=0). When the surface becomes increasingly rough radiation is scattered over an increasingly wider angle and a larger portion of the incident power is scattered in the backward direction. Roughness, in this context, means roughness in relation to the wavelength and is usually described with the parameters $k\sigma$ for 'normalized' height variation and $kl_{x,y}$ for 'normalized' horizontal roughness.

Modelling of the backscatter $\sigma^0(f, \theta_i)$ of random rough surfaces is a tedious task and (numerical) simulations are computationally prohibitive. So-called 'exact' solutions have been utilized to investigate the usefulness of simple first- and second-order solutions. To date three models are commonly used: the small perturbation (SMP) model for 'smooth' surfaces, the physical optics (PO) model for 'intermediate rough' surfaces and the geometrical optics (GO) model for 'very rough' surfaces. The validity ranges for these models are expressed in terms of the relative roughness parameters $k\sigma$ and kl and also in terms of the r.m.s. surface slope given by $m = \sqrt{2}\sigma/l$. The following validity conditions are recommended for surfaces that can be described adequately with Gaussian autocorrelation functions (Chen and Fung, 1988):

small perturbation model: $kl < 3$, $k\sigma < 0.3$, $m < 0.3$
physical optics model: $kl > 6$, $l^2 > 2.76\sigma\lambda$, $m < 0.25$
geometrical optics model: $kl > 6$, $l^2 > 2.76\sigma\lambda$, $(2k\sigma \cos\theta_i)^2 > 10$

The small perturbation model

The first order perturbation theory gives the like-polarized backscatter coefficients as (Ulaby et al.,1986):

$$\sigma^0_{pp}(f, \theta_i) = |\alpha_{pp}(\theta_i)|^2 \, 8 \, k^4 \cos^4\theta_i \, W(2 \, k \sin \theta_i) \qquad [31]$$

with

$$\alpha_{hh}(\theta_i) = R_{hh}(\theta_i) = \frac{\cos\theta_i - \sqrt{\varepsilon_r - \sin^2\theta_i}}{\cos\theta_i + \sqrt{\varepsilon_r - \sin^2\theta_i}}, \qquad [32]$$

which is the Fresnel reflectivity for horizontal polarization, and

$$\alpha_{vv}(\theta_i) = (\varepsilon_r - 1)\frac{\sin^2\theta_i - \varepsilon_r(1 + \sin^2\theta_i)}{(\varepsilon_r\cos\theta_i + \sqrt{\varepsilon_r - \sin^2\theta_i})^2}. \qquad [33]$$

The cross-polarized backscatter coefficient can be found by developing the small perturbation theory up to second order (Valenzuela, 1967), and is given as:

$$\sigma^0_{pq}(f,q_i) = \frac{2}{\pi} k^4 \sigma^4 \cos^2\theta_i \; |(\varepsilon_r - 1)(R_{vv} - R_{hh})|^2$$
$$\int_{-\infty}^{\infty} \frac{u^2 v^2}{|D_0|^2} W(u - k\sin\theta_i, v)\, W(u + k\sin q_i, v)\, du\, dv) \qquad [34]$$

with $D_0 = \sqrt{\varepsilon_r k^2 - u^2 - v^2} + \varepsilon_r\sqrt{k^2 - u^2 - v^2}$.

The physical optics model

The first order solution of the physical optics model yields expressions for the like-polarized backscattering coefficients:

$$\sigma^0_{pp}(f,\theta_i) = |R_{pp}(\theta_i)|^2 2k^2\cos^2\theta_i \exp(-4k^2\sigma^2\cos^2\theta_i) M_n$$
$$+ [|R_{pp}(\theta_i)|^2 \sin\theta_i + \mathrm{Re}(R_{pp} R^*_{ppl})\cos\theta_i] \; 2k \exp(-4k^2\sigma^2\cos^2\theta_i) M_s \qquad [35]$$

where R_{pp} is the Fresnel reflection coefficient for polarization pp, and $R_{ppl}{}^*$ the complex conjugate of the modified Fresnel reflection coefficient , which is related to the Fresnel reflection coefficients as:

$$R_{hhl}(\theta_i) = \frac{-2\sin\theta_i R_{hh}}{\cos\theta_i + \sqrt{\varepsilon_r - \sin^2\theta_i}} \qquad [36]$$

for horizontal polarization, and

$$R_{vvI}(\theta_i) = \sin\theta_i \frac{R_{vv}(1+\varepsilon_r) + (1-\varepsilon_r)}{\varepsilon_r \cos\theta_i + \sqrt{\varepsilon_r - \sin^2\theta_i}} \quad [37]$$

for vertical polarization respectively.

The terms M_n and M_s are given as:

$$M_n = \sum_{n=1}^{\infty} \frac{(4k^2\sigma^2\cos^2\theta_i)^n}{n!} \int_0^{\infty} \rho^n(\xi) J_0(2k\xi\sin\theta_i).\xi d\xi \quad [38]$$

and

$$M_s = \sum_{n=0}^{\infty} \frac{(4k^2\sigma^2\cos^2\theta_i)^{n+1}}{n!} \int_0^{\infty} \rho^n(\xi) \frac{\partial\rho}{\partial\xi} J_1(2k\xi\sin\theta_i)\,\xi\,d\xi \quad [39]$$

where $J_0(2k\xi\sin\theta_i)$ and $J_1(2k\xi\sin\theta_i)$ denote the zero- and first-order Bessel functions, respectively. The quantity $\rho(\xi)$ (identical to $C(\xi)$) is the autocorrelation function.

The first order solution of the physical optics model does not yield expressions for the depolarized backscatter, i.e. $\sigma_{hv} = \sigma_{vh} = 0$.

Geometrical optics model

The geometrical optics model is given in the form,

$$\sigma^0_{pp}(f,\theta_i) = |R_{pp}(0)|^2 \frac{\exp(-\tan^2\theta_i/2m^2)}{2m^2\cos^4\theta_i} \quad [40]$$

In the model the Fresnel reflectivity is evaluated at normal incidence. Therefore, it predicts no difference in HH and VV polarized backscatter. Also the first order geometric optics solution does not provide expressions for the cross-polarized backscattering .

4. ON THE SURFACE RESISTANCE - SOIL WATER CONTENT RELATIONSHIP

4.1 Comparison of surface resistance with onground observed soil water content

Land Surface Models require in one way or another a relation between evaporation and soil wetness (or 'degree of saturation'). Most developers of Land Surface Models have simply assumed a linear relationship between the water storage of a grid cel and the actual evaporation away from it. On a soil physical basis, it is easy to recognize that such relationship is oversimplified. However, aggregation of several non-linear systems does not guarantee a particular non-linear behaviour at a larger scale. The availability of data on the overall trend for a grid or region can therefore be recognized as being the major bottleneck to the solution of the shape of the relationship between r_s and θ for heterogeneous landscapes. Latter identified problem might be solved when r_s and θ are studied for composite terrain on the regional level as indicated within the present study.

In this paragraph we investigate the agreement between remote sensing r_s estimates with a limited number of in-situ soil moisture measurements. A comparison was made between a single pixel and a single soil moisture plot (Fig. 12A). In this way, a bias is introduced because the spatial scales of a pixel, being 18,5 * 18,5 m^2 and the areal size of a plot, being 2 * 2 m^2 are not matched. The total number of plots taken into account was 44. To encompass this scale discrepancy, values were plotted on the parcel scale as well (Fig. 12B). The scatter consideraby decreases both for r_s and θ when considering parcels instead of individual plots. The moisture values were taken from a depth of 10 cm. The conclusion from this experiment is that the relation between r_s and θ is also non-linear by nature at composite terrain and that effects of soil coverage, leaf area index, air temperature and vapour pressure deficit on r_s are of less importance. Otherwise, R^2 for parcels comprising vineyard, wheat, maize and fallow land in various hydrological states and at a spatial scale of 500 km^2 should have been less (R^2=0.93). The curve could be fitted with r_s=exp(7.8-17.5θ_{10}).

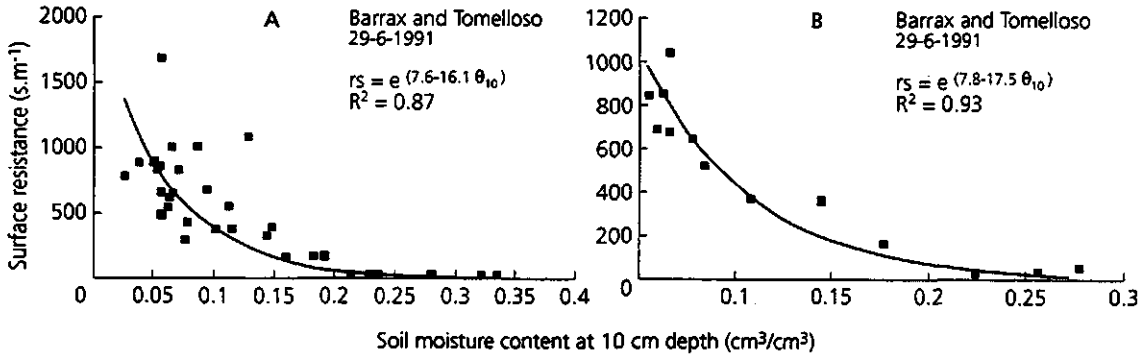

Fig. 12: Trend between SEBAL based evaporation resistance values and field soil water content at 10 cm depth. (12A) $r_s(\theta)$ relation for the total plots network and (12B) $r_s(\theta)$ relation at parcel level.

4.2 Comparison of backscatter coefficients with onground soil water content and soil roughness.

Data available

Calibrated AIRSAR data of Barrax were made available by the Jet Propulsion Laboratory (JPL) of NASA for a preliminary study on the usefulness of radar data. Figures 13 and 14 show a detail of these images, presented as a multi-band HH-polarized colour composite, for the observation dates 19 June 1991 and 14 July 1991, respectively.

Table 1 and figure 13 show the selected fields at the Barrax site. Ground observations have been made at fields 1 to 9. Figure 15 illustrates a result of surface roughness measurement for a maize field in Barrax. A large field with a central pivot irrigation system was selected for its variation in radar backscatter (segments 1 to 4), presumably related to the elapsed time after irrigation. Also at the Tomelloso site observations were made. However, since AIRSAR radar data are not yet available this site had to be excluded from the preliminary study.

Soil moisture measurements were restricted to June 19 and to four fields (2, 4, 5 and 7) at the Barrax site and three fields at the Tomellose site. Complementary soil moisture data acquired by JPL at July 14 have not been made available yet. These constraints limit the analysis possibilities significantly for the moment.

Models used

For the description of rough surface scattering two bare soil models were used. These are the Integral Equation Method (IEM) model (Fung et al., 1992) and an empirical model developed by Oh, Sarabandi and Ulaby (Oh et al., 1992) which will be referred to as the OSU model. To relate soil dielectric constant to volumetric soil moisture content the model of Wang (Wang and Schmugge, 1980) will be used. Figure 16 illustrates the relation between ε_r and volumetric water content for a typical soil found in Barrax for the three AIRSAR frequency bands.

The IEM model combines the small perturbation (SMP) and the Kirchhoff approaches (GO and PO) and has a larger overall applicability. For the ranges of applicability given in section 3.2.2 the IEM model is shown to break down in the corresponding models.

Airsar multi-frequency HH-polarized image (P-band: blue, L-band: green, C-band: red) La Mancha - Barrax 19-06-91

Fig. 13

Airsar multi-frequency HH-polarized image (P-band: blue, L-band: green, C-band: red) La Mancha - Barrax 14-07-91

Fig. 14

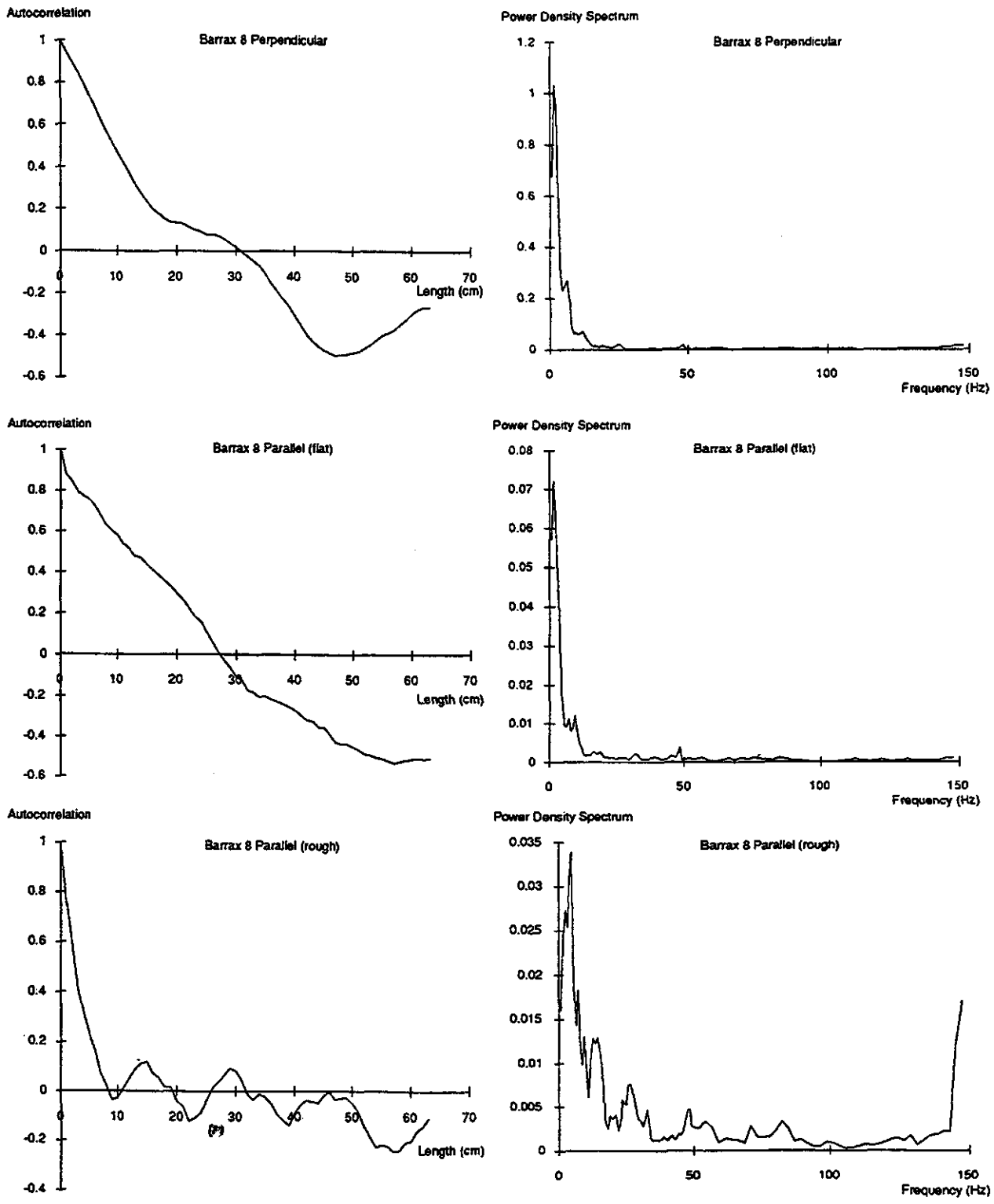

Fig. 15: Autocorrelation functions and power spectral density functions of field BA-8 (maize).

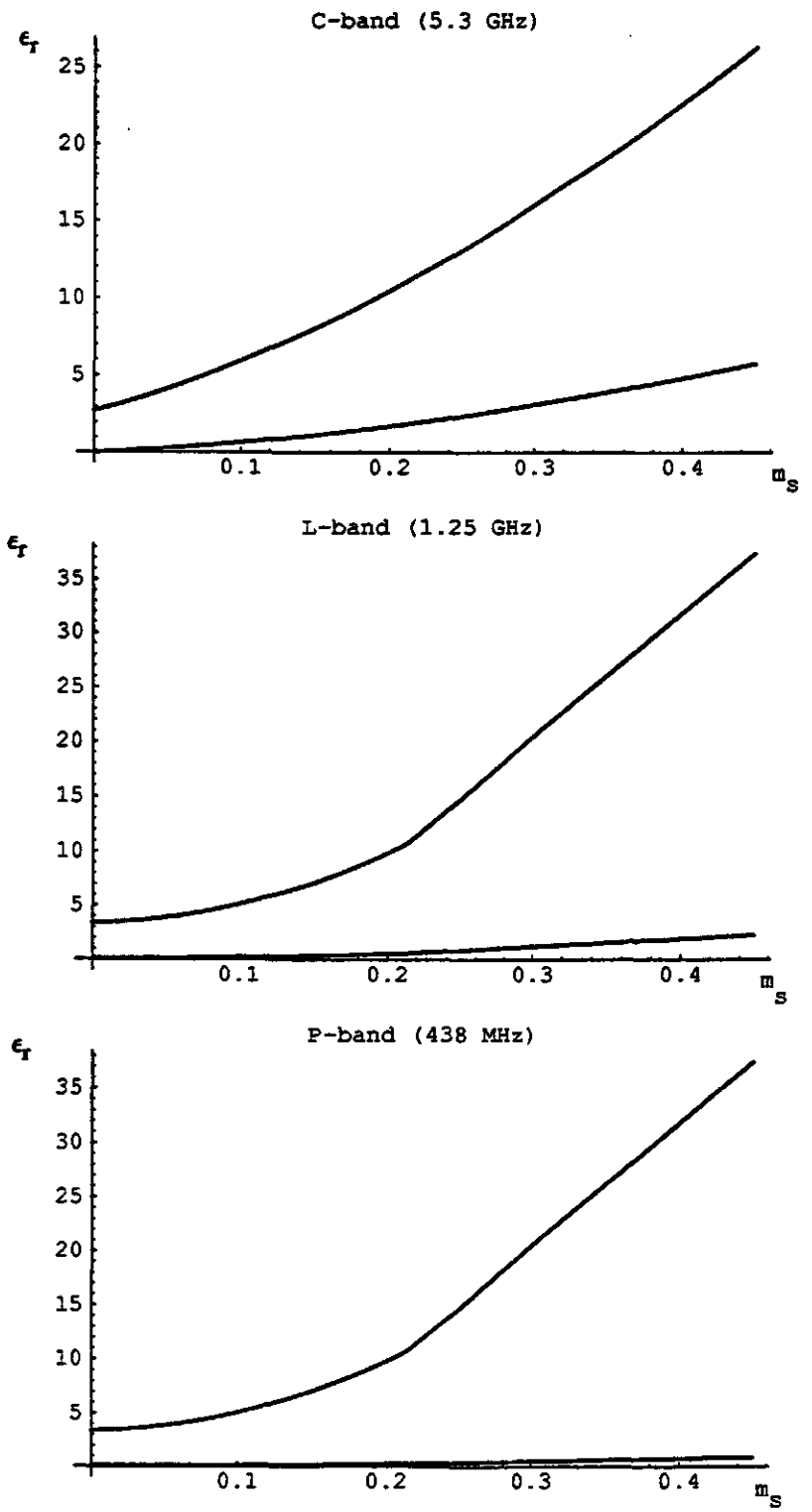

Fig. 16: Dielectric constant as function of volumetric soil moisture for C-, L- and P-band. The upper curves relate to the real part, the lower to the imaginary parts of ϵ_r. (Soil texture: clay 10%, silt 65%, sand 25%, soil bulk density 1.4.)

Table 1. Field description for the Barrax site.

(a) Field type, 19 June 1991

1:	Barrax #1	irrigated maize
2:	Barrax #2	bare soil
3:	Barrax #3	Non-irrigated barley (stubble-field)
4:	Barrax #4	irrigated alfalfa
5:	Barrax #5	irrigated maize
6:	Barrax #6	Non-irrigated barley
7:	Barrax #7	irrigated barley
8:	Barrax #8	irrigated maize
9:	Barrax #9	bare soil
10:	Barrax	segment #1 circle
11:	Barrax	segment #2 circle
12:	Barrax	segment #3 circle
13:	Barrax	segment #4 circle

(b) Incidence angle and number of pixels for June 19 and July 14 repectively.

	06/19: inc	pix	07/14: inc	pix
1:	47.9	422	40.1	505
2:	44.4	211	35.8	133
3:	53.9	258	47.8	315
4:	39.0	332	29.1	424
5:	38.2	233	30.6	204
6:	53.7	162	47.5	118
7:	53.9	146	47.8	108
8:	42.2	442	33.2	386
9:	39.5	156	28.4	484
10:	43.7	896	35.4	456
11:	44.9	586	36.8	862
12:	45.1	691	37.1	688
13:	45.7	843	37.7	587

(c) Volumetric soil moisture data for fields 2/4/5/7 at several depths (cm) for 19 June.

depth:	2	5	10	20	25	30
2:	-	3.4	7.1	-	-	16.0
4:	23.1	30.6	32.2	-	-	-
5:	13.0	18.6	26.1	-	-	-
7:	-	5.4	9.7	12.2	14.0	-

(d) Soil roughness data *ks* (cm) and *kL* (cm) for 19 June.

	ks:			kL:		
	C	L	P	C	L	P
1:	1.4	0.33	0.12	9.1	2.1	0.75
2:	1.6	0.37	0.13	4.4	1.0	0.37
3:	1.7	0.40	0.14	9.2	2.2	0.76
4:	0.6	0.15	0.05	12.5	3.0	1.04
5:	2.0	0.47	0.16	11.0	2.6	0.91
6:	1.0	0.23	0.08	5.3	1.3	0.44
7:	1.1	0.26	0.09	16.9	4.0	1.40
8:	1.9	0.45	0.16	11.7	2.7	0.96
9:	1.7	0.40	0.14	16.1	3.7	1.33

The OSU model is an empirical model based on the physical basis given in section 3.2.2 and also has a fairly large range of applicability. Values for the scaled roughness parameter *ks* should be in the range of 0.1 to 6 and for *kL* in the range of 2.6 to 19.7. This empirical model can be inverted to estimate soil dielectric constant and roughness. It is shown to yield good results for *ks* values up to 3. For larger *ks* values, that is for rough (compared to wavelentgh) surfaces, the inverse model is not sensitive for roughness (i.e. *ks*) changes anymore. The inverse model will be referred to as the INVOSU model.

The models apply to bare fields, almost (i.e. effectively) bare fields or to fields with completely dried out vegetation which become transparant to microwaves, such as fully ripened cereals. A problem in Barrax is the presence of sprinklers. These metal vertical structures may cause an increase in the backscatter, notably for the VV term. Since the inversion algorithm is based on HH/VV and HV/VV backscatter ratios for single frequencies these sprinklers may lead to erroneous results. An alternative inversion approach, not studied here, is the use of single polarized (in this case HH) multi-frequency data.

In the soil data collection report (Vissers and Hoekman, 1991) the fields are described in more detail. For field 2, the bare soil field, sprinklers are absent and the models apply. Field 4 has a 60% coverage of alfalfa and sprinklers; field 5 has sprinklers but the maize plants are small, the coverage is only 5%; field 7 has no sprinklers, the vegetation cover is 40% but the barley plants are fully ripened. Also for field 7 the models should apply. In summary: the models should apply for field 2 and 7, and may apply to a lesser extent to field 5.

Results

Table 2 shows the observed values of the radar backscatter for three bands and three polarizations for fields 2, 4, 5 and 7 at June 19. The predictions of the IEM model and OSU model agree well with the observed values for field 2 and 5 and to a lesser extent to field 7. The OSU model yields slightly better results, even though the range of validity for *kL* is exceeded in the L-band for field 2 and in the P-band for all fields (see table 1.d).

The values of measured soil moisture (table 1.c) can now be compared with the results of the INVOSU model (table 3). The model is applied for all fields at all frequency bands and at both dates. Subsequently the results for the estimation of *ks*, (amplitude of) dielectric constant ε, the difference *d* between the observed backscatter and predicted backscatter using the estimated *ks* and ε values and the estimated volumetric soil moisture using Wang's model, are shown.

For most C-band data and some P-band data the algorithm is non-applicable. Furthermore, as can be seen in table 1.d the kL figures are out of range for all P-band data and the L-band data of fields 1, 2, 3 and 6.

In general, because of the limited range of applicability and the presence of sprinklers and well-developed crops, the results of soil moisture estimation, can not be expected to be very accurate under the present conditions. In June for field 2 volumetric soil moisture (m_s) was estimated at 11% and 18% for L- and P-band respectively. These compare with the observed values of 3.4% (at 5 cm depth), 7.1% (at 10 cm) and 16.0% (at 30 cm). The higher percentage found for P-band can be related to the larger penetration depth. For an effective soil moisture content of 10% these can be calculated as 165 cm in P-band and 40 cm in L-band (see section 3.2.2). For field 4 the inversion models used here do not apply. For field 5 soil moisture was estimated at 13% and 17% for L- and P-band, respectively, which compares with the observations of 13% (at 2 cm), 18.6% (at 5 cm) and 26.1% (at 10 cm). For field 7 the result of 10% in L-band compares with the observations of 5.4%, 9.7%, 12.2 % and 14% at depths of 5, 10, 20 and 25 cm, respectively. The estimation agrees well with the measured values averaged over the penetration depth (approx. 40 cm).

Also the results for the circle segments, i.e. field numbers 10 to 13, appear reasonable. Vegetation information is still absent, however, the field is likely to comprise maize simular to field 5. As can be seen in the image the central pivot system has sprinkled segment 2 (which appears bright) and will sprinkle segment 1 next (which appears dark). The contrast between the four segments is the highest between segment 1 and 2 (filed 10 and 11) for which soil moisture in L-band was estimated at 27% and 12%, respectively. In P-band the results for these two segments are 25% and 18%. The P-band measures the soil over a much thicker volume, hence it can be expected that the contrast observed in L-band (15% absolute) is leveled out in P-band (to 7% absolute).

Conclusion

Considering the various factors which limit the applicability of the microwave backscatter models used and the very limited data set available until now, the results are promising. Both qualitatively and quantitatively the estimations of soil moisture compare well with the field observations or the expected values. A multi-frequency approach and correction for vegetation influence may improve the results as well as enlarge the applicability of soil moisture estimators even further.

Table 2. Results of σ^0 observations and predictions by two models for fields 2/4/5/7 at 19 June 1991.

(a) Observed σ^0

C-HH	C-VV	C-HV	L-HH	L-VV	L-HV	P-HH	P-VV	P-HV
-13.03	-13.73	-23.34	-21.50	-19.57	-36.68	-25.46	-22.37	-38.34
-7.20	-9.52	-15.65	-16.24	-14.55	-28.57	-26.74	-20.59	-35.34
-8.64	-9.30	-17.25	-17.05	-15.47	-31.88	-23.46	-21.47	-36.17
-12.99	-15.39	-22.86	-24.40	-22.87	-36.47	-28.39	-24.31	-29.50

(b) Predicted σ^0 by IEM model

C-HH	C-VV	L-HH	L-VV	P-HH	P-VV
-10.7	-12.9	-20.7	-16.5	-32.3	-28.1
-16.5	-13.2	-23.9	-19.0	-31.4	-26.4
-7.4	-10.0	-15.4	-11.9	[illegible]	-19.3
-18.4	-19.4	-29.6	-24.3	-35.8	-29.9

(c) Predicted σ^0 by OSU model

C-HH	C-VV	C-HV	L-HH	L-VV	L-HV	P-HH	P-VV	P-HV
-13.7	-13.5	-26.0	-22.7	-22.1	-38.7	-30.7	-30.0	-50.6
-14.4	-12.1	-24.5	-25.4	-21.6	-39.1	-34.2	-29.9	-51.9
-9.6	-9.3	-20.1	-17.7	-16.4	-30.8	-26.0	-24.3	-42.7
-17.0	-16.4	-29.4	-27.3	-25.8	-43.4	-35.6	-33.8	-55.7

Table 3. Results of the inverse use of OSU model for all fields and both dates. The parameter *ks* is the estimation of scaled roughness, ε the estimation of dielectric constant, d the difference between σ^0 observation and prediction using the estimated values and m_s is the estimated volumetric soil moisture content.

(a) C-band June

	ks	ε	*d*	m_s
1-13	not applic.			

(b) L-band June

	ks	ε	*d*	m_s
1	0.24	7.6	8.8	16
2	0.22	5.7	3.4	11
3	0.45	5.4	-2.8	10
4	0.45	7.6	1.2	16
5	0.26	6.3	5.0	13
6	0.73	8.7	-7.0	18
7	0.67	5.1	-5.0	10
8	1.21	6.2	-2.2	13
9	0.09	5.3	13.0	10
10	0.17	6.1	13.9	12
11	0.14	17.1	13.3	27
12	0.13	16.1	12.4	26
13	0.13	9.5	14.5	19

(c) P-band June

	ks	ε	*d*	m_s
1	0.08	8.1	16.0	17
2	0.24	8.8	-2.1	18
3	0.87	64513.9	-19.7	-
4	0.20	59.5	-5.3	wet
5	0.36	8.2	-4.6	17
6	n.a.			
7	n.a.			
8	0.31	21.6	-4.3	31
9	0.25	6.2	2.0	13
10	0.03	9.0	22.4	18
11	0.07	15.7	11.9	25
12	0.06	12.4	12.6	22
13	0.04	9.6	18.5	19

(d) C-band July

	ks	ε	*d*	m_s
1	n.a.			
2	1.0	5.3	0.9	10
3-4	n.a.			
5	0.8	4.3	4.7	7
6-8	n.a.			
9	1.0	4.7	2.6	9
10-13	n.a.			

(e) L-band July

	ks	ε	*d*	m_s
1	0.20	4.8	23.6	9
2	0.26	7.0	2.7	14
3	0.29	7.6	-0.5	16
4	0.80	6.9	-6.2	14
5	0.07	7.2	19.2	15
6	0.79	7.3	-8.0	15
7	0.32	8.3	-1.5	18
8	1.70	16.9	-0.7	26
9	0.20	6.1	8.4	12
10	0.16	8.9	21.2	18
11	0.21	9.7	17.0	19
12	0.14	11.4	21.7	22
13	0.20	6.6	21.4	14

(f) P-band July

	ks	ε	*d*	m_s
1	n.a.			
2	0.23	6.8	-1.6	14
3	0.62	12.1	-13.0	22
4	0.39	17.1	-10.0	27
5	0.08	4.6	15.6	8
6	0.53	12.4	-11.9	22
7	0.33	8.4	-7.1	17
8	n.a.			
9	n.a.			
10	n.a.			
11	0.22	12.4	6.3	22
12	0.16	12.4	9.2	22
13	0.22	5.9	12.4	12

5. CONCLUDING REMARKS

The results of the remote sensing experiment carried out at partially covered land in the Mediterranean Spanish climate consist of (i) the estimation of the spatial variability of the surface heat exchange rates, (ii) the assessment of the spatial variability of the surface resistance regulating the actual evaporation rate and (iii) the spatial variability of top soil water content.

It has been demonstrated that different hydro-meteorological systems function in the Tomelloso and Barrax area. Albeit their areal mean values of Normalized Difference Vegetation Index and surface albedo are identical, their range is not. The $T_0(r_0)$ relationship was recognized as being a suitable tool to identify partial areas or clusters which behave hydrologically similar.

It has been further shown that an array of NDVI-r_0-T_0 data is suitable to describe the land surface energy budget in quantitative terms. Although the regional validation with surface fluxes and microwave data has not yet been completed, a relationship with the regional soil moisture could be found. Remote estimates of r_s appeared to be satisfactory correlated with soil moisture observations at 10 cm depth for parcel averaged values. It was finally concluded, that the relationship between total resistance to evaporation and soil water content is not linear for composite land surfaces. The areal average land surface evaporation arising at mesoscale in a Mediterrenean climate like Spain can be approached from the areal average soil water content at 10 cm depth using $r_s = \exp(7.8\text{-}17.5\theta_{10})$

Considering the various factors which have limited the applicabilty of the microwave models used in this study and the limited data set available for this study until now, the results can said to be promising. Quantitative estimations of surface layer soil moisture content compare well with field observations. Also indications that P-band assesses soil moisture content over a much deeper surface layer, which may be in excess of one meter, have been obtained. Further improvements are foreseen when soil moisture estimators are used utilizing multi-frequency data instead of single frequency multi-polarized data. Also the influence of a vegetation cover should be considered in more detail. The latter may be achieved either by using the information contained in the microwave data themselves and/or using optical data.

Future analysis, therefore, should include elaboration of the microwave research as well as extension of the experimental data set as soon as these are available. These comprise amongst

others the AIRSAR radar data of Tomelloso, a low resolution AIRSAR radar strip covering the area from Barrax until Tomelloso and soil moisture data collected by NASA during the second overpass of the AIRSAR.

The other point of interest for future work is the combination of optical reflectance, infrared thermal emission and radar data at these test sites to establish the ultimate link between energy balance (by means of surface resistance) and soil water balance (by means of soil water content).

Acknowledgements The investigation was made possible with financial support of the European Community, the International Hydrological Programme of UNESCO and The Netherlands Board of Remote Sensing. The authors are indebted to J.N.M. Stricker and P. Droogers of Wageningen Agricultural University who collected the in-situ moisture data and made them available to the data analysis of the NS001 images. The suggestions given by M. Menenti on the manuscript are appreciated. The authors are grateful to A.J. Dolman (Winand Staring Centre) and G. Lemoine (Joint Research Centre) who reviewed the first draft version of this report.

REFERENCES

American Meteoroloical Society, 1991. 10th Conference on Biometeorology and aerobiology, special session on hydrometerology, September 10-13, 1991, Salt Lake City, Utah.

Bastiaanssen, W.G.M., 1990. Mapping vapour and heat transport coefficients in soil and air using Landsat observations in arid regions, Proc. IGARSS 1990, Univ. of Maryland, USA, May 20-24: 1845-1849.

Bastiaanssen, W.G.M. 1993. Regionalization of surface fluxes and Moisture Indicators at composite terrain, Ph.D. Thesis, Wageningen Agricultural University, The Netherlands (in prep.).

Becker, F., H.J. Bolle and P.R. Rowntree, 1988. The International Satellite Land-Surface Climatology Project, United Nations Environmental Programme, Neue Presse Verlags-Gmbh, Passau, F.R.G.: pp. 100.

Bolle, H.J. & Streckenbach, B. (1992) The ECHIVAL field experiment in a desertification-threatened area EFEDA. First Annual Report to EC, Published by the EFEDA-Secretariat, Free University of Berlin, Berlin, Germany.

Chen, M.F. and A.K. Fung, 1988, A numerical study of the regions of validity of the Kirchhoff and small-perturbation rough surface scattering models, Radio Science, Vol.23, pp.163-170.

Choudhury, B.J., 1989. Estimating evaporation and carbon assimilation using infrared temperature data: Vistas in modeling, in Theory and Applications of Optical Remote Sensing, (e2segd.) G. Asrar, John Wiley, New York: 628-690.

Dickinson, R.E., A. Henderson-Sellers, P.J. Kennedy and M.F. Wilson, 1986. Biosphere-Atmosphere Transfer Scheme (BATS) for the NCAR Community Climate Model, NCAR Technical Note NCAR/TN-275+STR.

Dolman, A.J., 1992. A note on areally-averaged evaporation and the value of the effective surface conductance, J. of Hydr. 138: 583-589.

Engman, T. and R.J. Gurney, 1991. Remote sensing in hydrology, London.

Feddes, R.A., M. Menenti, P. Kabat and W.G.M. Bastiaanssen, 1992. Is large scale inverse modelling of unsaturated flow with areal average evaporation and surface soil moisture as estimated from remote sensing feasible? J. of Hydr. 143 (special issue) Modelling flow and transport in the unsaturated zone: scale problems and spatial variability: pp. 125-152.

Fung, A.K., L. Zongqian and K.S. Chen, 1992, Backscattering from a randomly rough dielectric surface, IEEE Transactions on Geoscience and Remote Sensing, Vol.30, pp.356-369.

Griend, van de, A.A., P.J. Camillo and R.J. Gurney, 1985. Discrimination of soil physical parameters, thermal inertia and soil moisture from diurnal surface temperature fluctuations, Water Resources Research, vol 21: 997-1009.

Griend, van de, A.A. & Owe, M. (1992) On the relationship between thermal emissivity and the Normalized Difference Vegetation Index for natural surfaces, Int. J. of Rem. Sensing (in press).

Jarvis, P.G., 1976. The interpretation of the variations in leaf water potential and stomatal conductance found in canopies in the field, Philos Trans R Soc London Ser B 273: 593-610.

Koepke, P., K.T. Kriebel and B. Dietrich, 1985. The effect of surface reflection and of atmospheric parameters on the shortwave radiation budget, Adv. Space Res. 5: 351-354.

Kong, J.A. (ed), 1990. Polarimetric remote sensing, Elsevier.

Menenti, M., 1984. Physical aspects and determination of evaporation in deserts applying remote sensing techniques, ICW report 10, special issue, The Winand Staring Centre, Wageningen. p. 202.

Menenti, M., Bastiaanssen, W.G.M., Eick, van, D. & Abd El Karim, M.A. (1989). Linear relationships between surface reflectance and temperature and their application to map actual evaporation of groundwater. *Adv. Space Res.* Vol **9**, No. **1**, 165-176.

Menenti, M., W.G.M. Bastiaanssen, K. Hefny and M.H. Abd El Karim, 1991. Mapping groundwater losses by evaporation in the Western Desert of Egypt, The Winand Staring Centre, Report 43, Wageningen, The Netherlands. pp. 116.

Monteith, J.L., 1965. Evaporation and the environment, In: The state and movement of water in living organisms, XIXth Symp. Soc for Xp. Biol, Swansea, Cambridge University Press: 205-234.

Moran, M.S. (1990) A satellite-based approach for evaluation of the spatial distribution of evapotranspiration from agricultural lands. Ph.D. thesis, University of Arizona, Tucson, USA.

Noilhan, J. and S. Planton, 1988. A simple parameterization of land surface processes for meteorological models, Mon. Weather Rev. 117: 536-549.

Oh Y., K. Sarabandi and F.T. Ulaby, 1992, An empirical model and an inversion technique for radar scattering from bare soil surfaces, IEEE Transactions on Geoscience and Remote Sensing, Vol.30, pp.370-381.

Owe, M. 1992. Measurements of surface resistance, reflectance and thermal emissivity during EFEDA, Proc. European Geophysical Society, Edinborough 1992, Supplement II to Vol. 10: C280.

Penman, H.L., 1948. Natural evaporation from open water, bare soil and grass, Proc. R. Soc. Land Ser. a 193: 120-145.

Schmugge T.J. and F. Becker, 1991. Remote sensing observations for the monitoring of land-surface fluxes and water budgets, in (eds.) Schmugge, T. and J.C. Andre, 1991. Land surface evaporation, measurement and parameterization, Springer Verlag: 337-347.

Seguin, B. and B. Itier, 1983. Using midday surface temperature to estimate daily evaporation from satellite thermal IR data. Int. J. of Rem. Sens. 4: 371-383.

Sellers, P.J., Y. Mintz, C. Sud and A. Dalcher, 1986. A simple Biosphere model (SiB) for use within general circulation models, J. Atm. Sci. 43: 505-531.

Shi, J. v. J.V. Soares, L. Hess, E.T. Engman, J.J. van Zijl, 1991, Soil Moisture measurements from airborne SAR, Proc. of the Third Airborne Synthetic Aperture Radar (AIRSAR) Workshop, 23-24 May 1991, Pasadena, JPL Publication 91-30, pp.68-77.

Sucksdorff, Y. & Ottle, C. (1990) Application of satellite remote sensing to estimate areal evapotranspiration over a watershed. J. Hydrol. 121: 321-333.

Tsang, L., J.A. Kong and R.T. Shin, 1985, Theory of microwave remote sensing, New York, Wiley.

Ulaby, F.T., R.K. Moore and A.K. Fung, 1982, Microwave Remorte Sensing, Vol.II, Addison-Wesley, Reading, Mass.

Ulaby, F.T. and C. Elachi (eds.), 1990. Radar polarimetry for geoscience applications, Artech House, London.

Van Zijl, J.J., 1989, Unsupervised classification of scattering behaviour using radar polarimetry data, IEEE Transactions on Geoscience and Remote Sensing, Vol.GE-27, pp. 36-45.

Vissers, M.A.M. and D.H. Hoekman, 1991, Soil data collection for the JPL-SAR campaign during EFEDA, Wageningen Agricultural University - CARTOSCAN report.

Wang J.R. and T.J. Schmugge, 1980, An empirical model for the complex dielectric permittivity of soil as a function of water content, IEEE Transactions on Geoscience and Remote Sensing, Vol.18, pp.288-295.

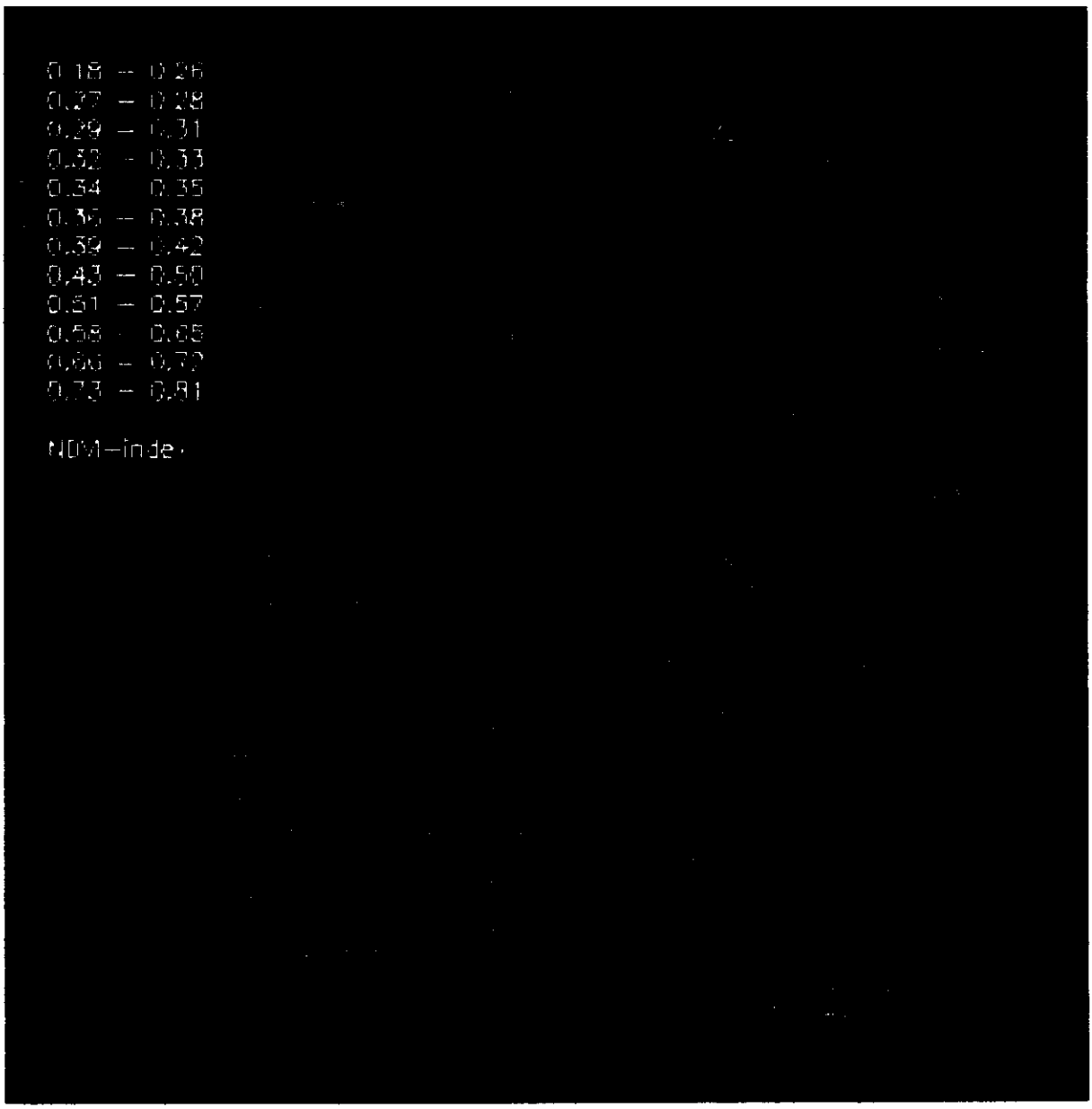
0.18 – 0.25
0.27 – 0.28
0.29 – 0.31
0.32 – 0.33
0.34 – 0.35
0.36 – 0.38
0.39 – 0.42
0.43 – 0.50
0.51 – 0.57
0.58 – 0.65
0.66 – 0.72
0.73 – 0.81
NDVI-index

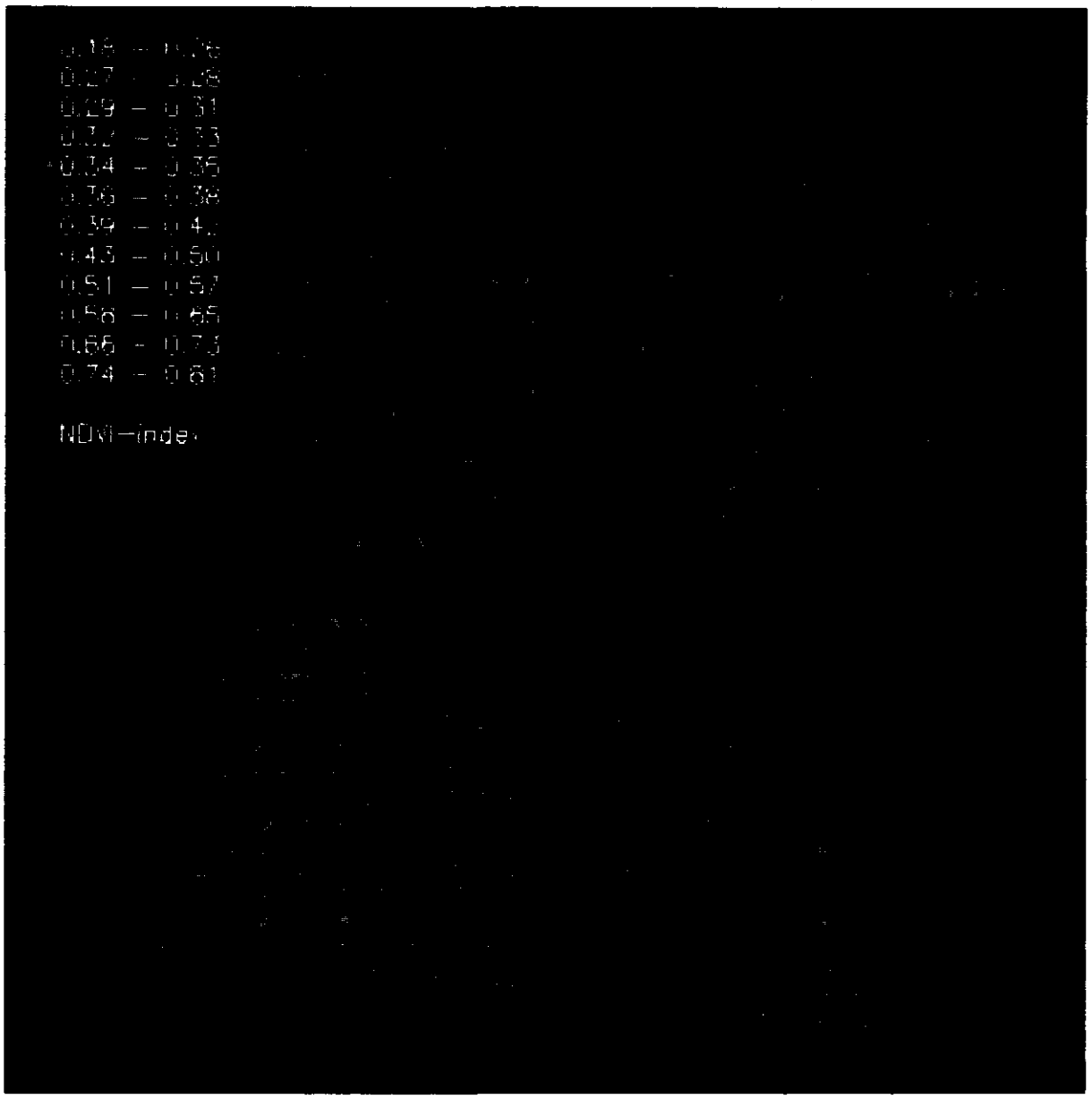
0.15 - 0.19
0.27 - 0.29
0.29 - 0.31
0.32 - 0.33
0.34 - 0.35
0.36 - 0.38
0.39 - 0.42
0.43 - 0.50
0.51 - 0.57
0.58 - 0.65
0.66 - 0.73
0.74 - 0.81
NDVI-Index

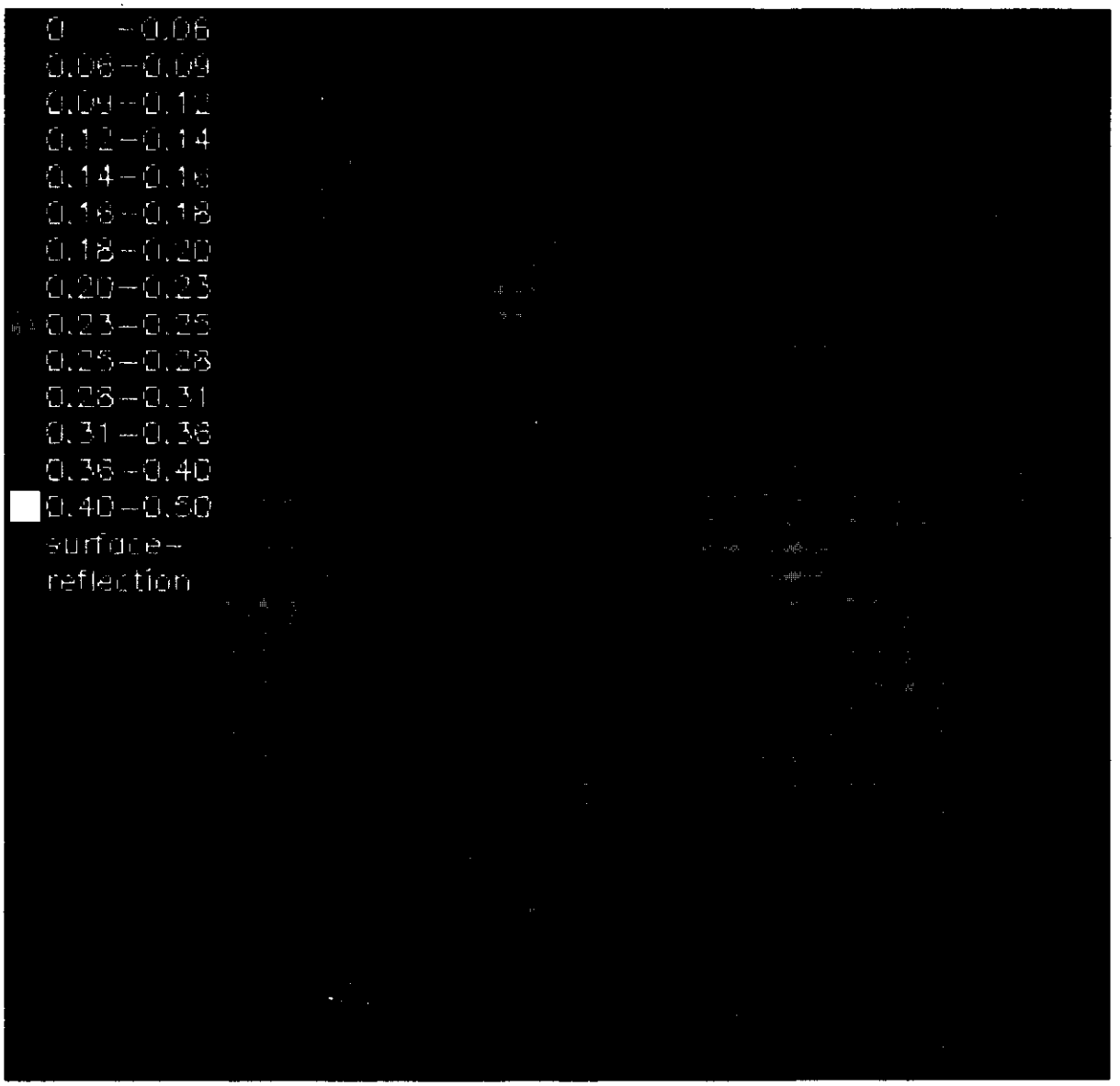
0 -0.06
0.06-0.09
0.09-0.12
0.12-0.14
0.14-0.16
0.16-0.18
0.18-0.20
0.20-0.23
0.23-0.25
0.25-0.28
0.28-0.31
0.31-0.36
0.36-0.40
0.40-0.50
surface-
reflection

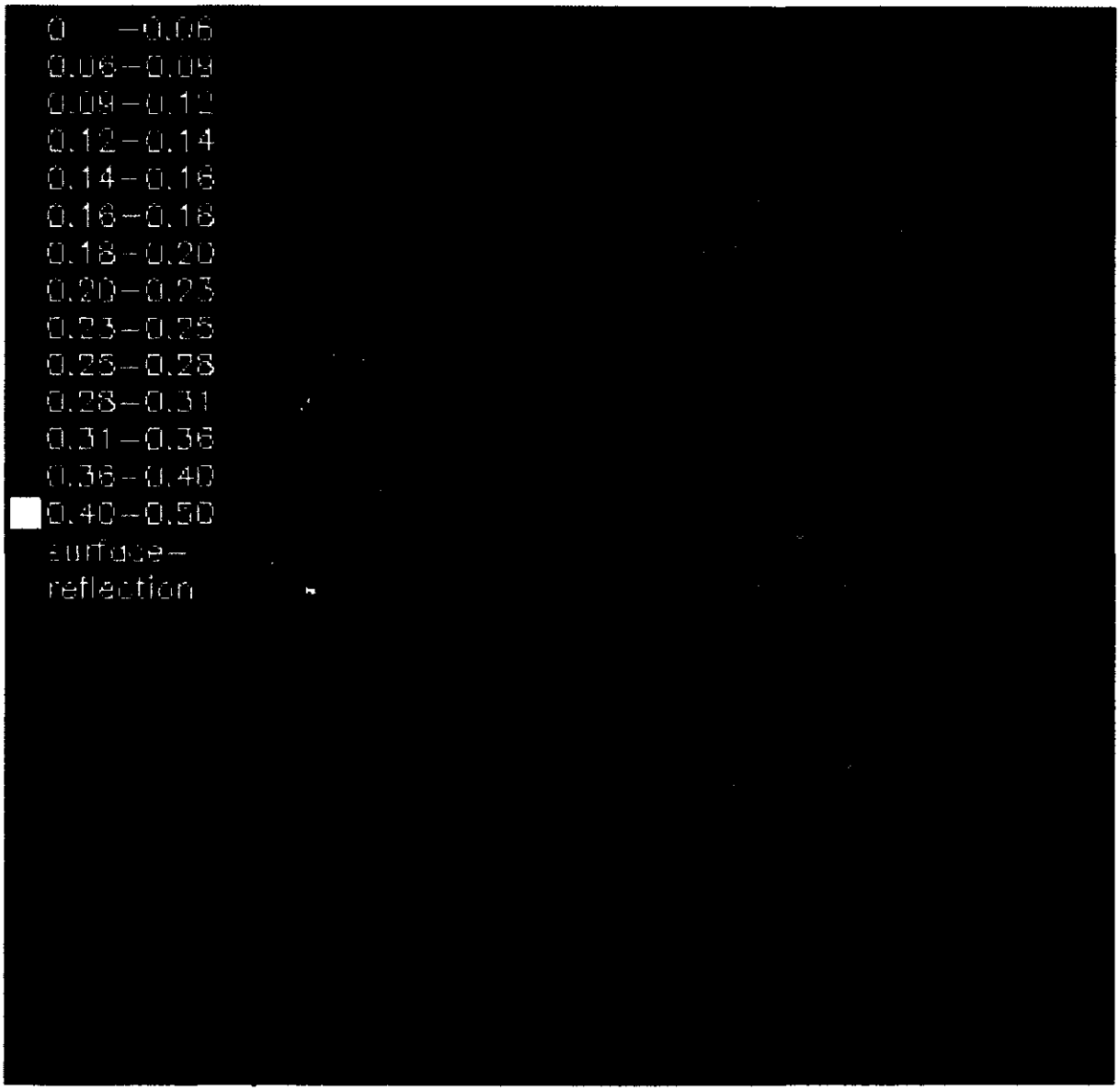
0 —0.06
0.06—0.09
0.09—0.12
0.12—0.14
0.14—0.16
0.16—0.18
0.18—0.20
0.20—0.23
0.23—0.25
0.25—0.28
0.28—0.31
0.31—0.36
0.36—0.40
0.40—0.50
surface—
reflection

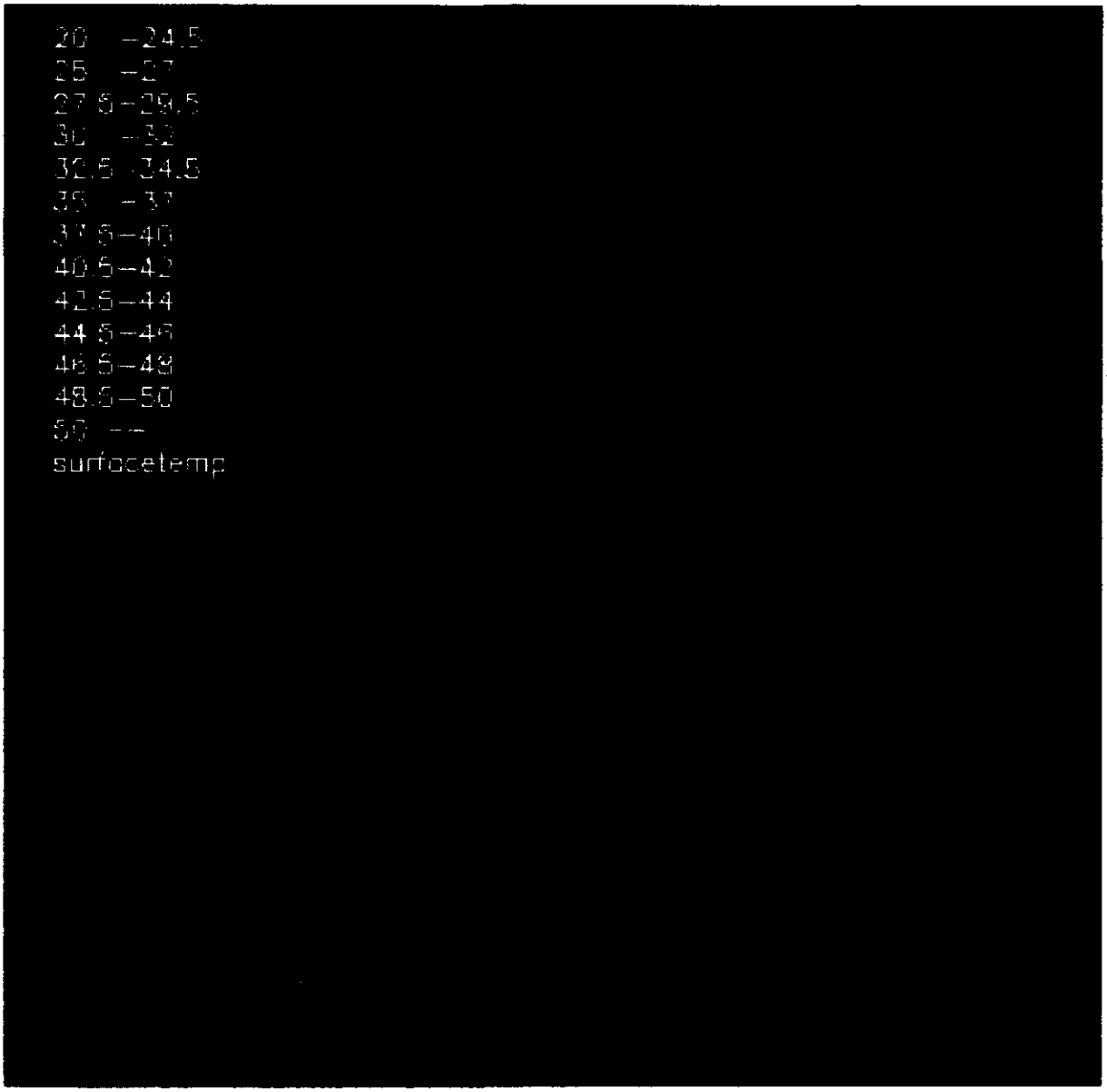
20 -24.5
25 -27
27.5-29.5
30 -32
32.5-34.5
35 -37
37.5-40
40.5-42
42.5-44
44.5-46
46.5-48
48.5-50
50 --
surfacetemp

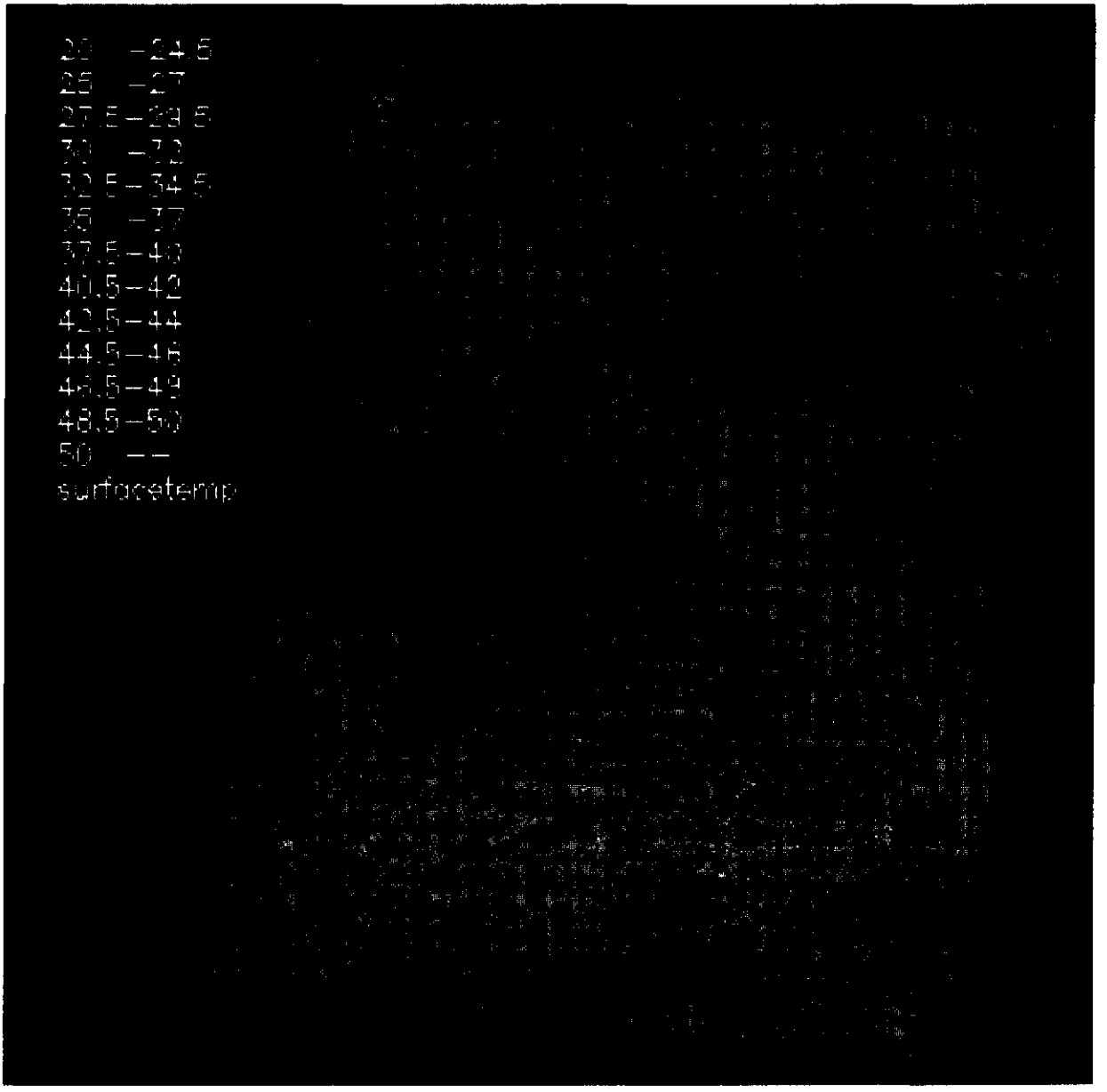
25 -24.5
27.5 -29.5
35 -37
37.5 -40
40.5 -42
42.5 -44
44.5 -46
46.5 -49
48.5 -50
50 --
surfacetemp

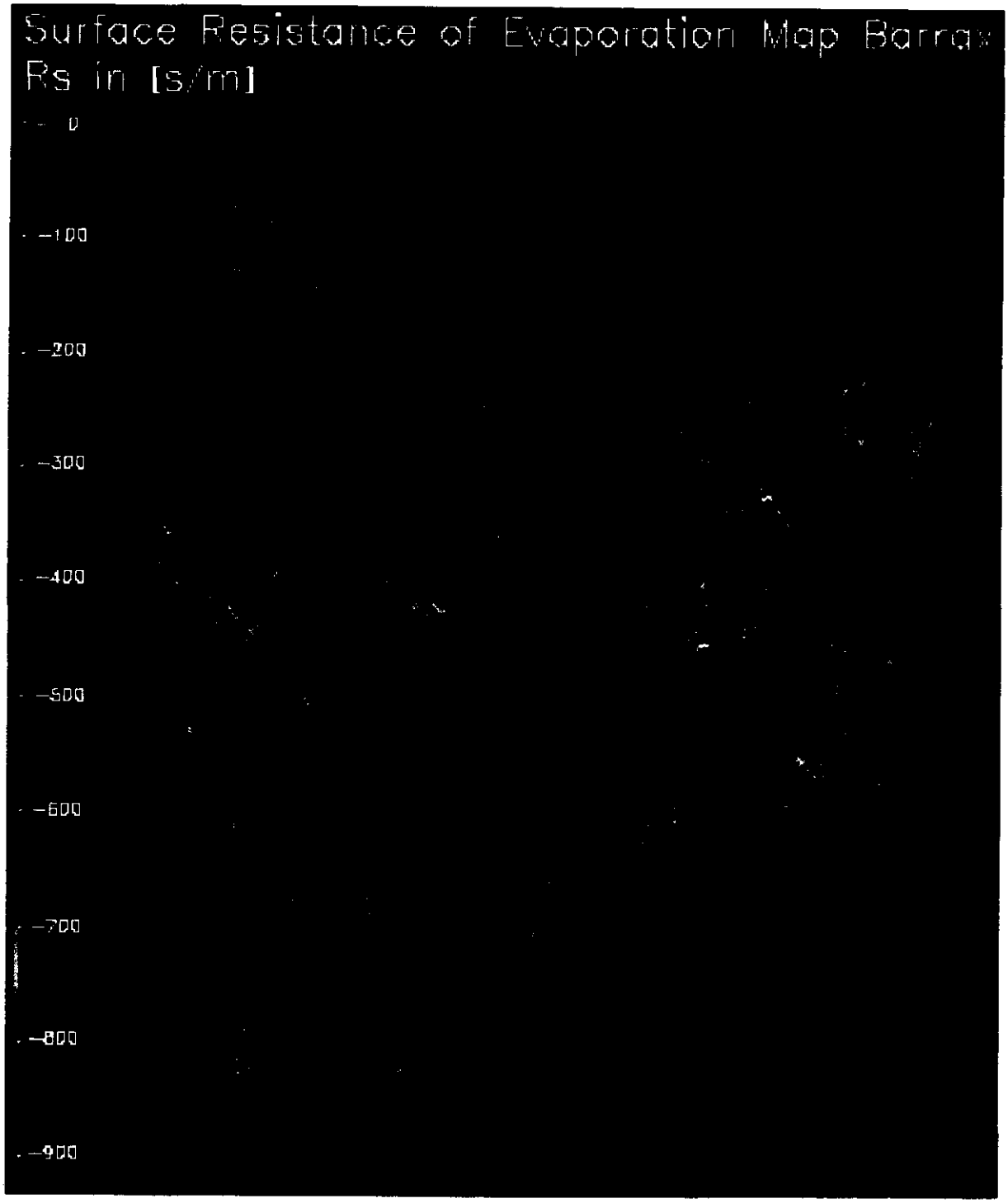
Surface Resistance of Evaporation Map Barra
Rs in [s/m]
0
-100
-200
-300
-400
-500
-600
-700
-800
-900

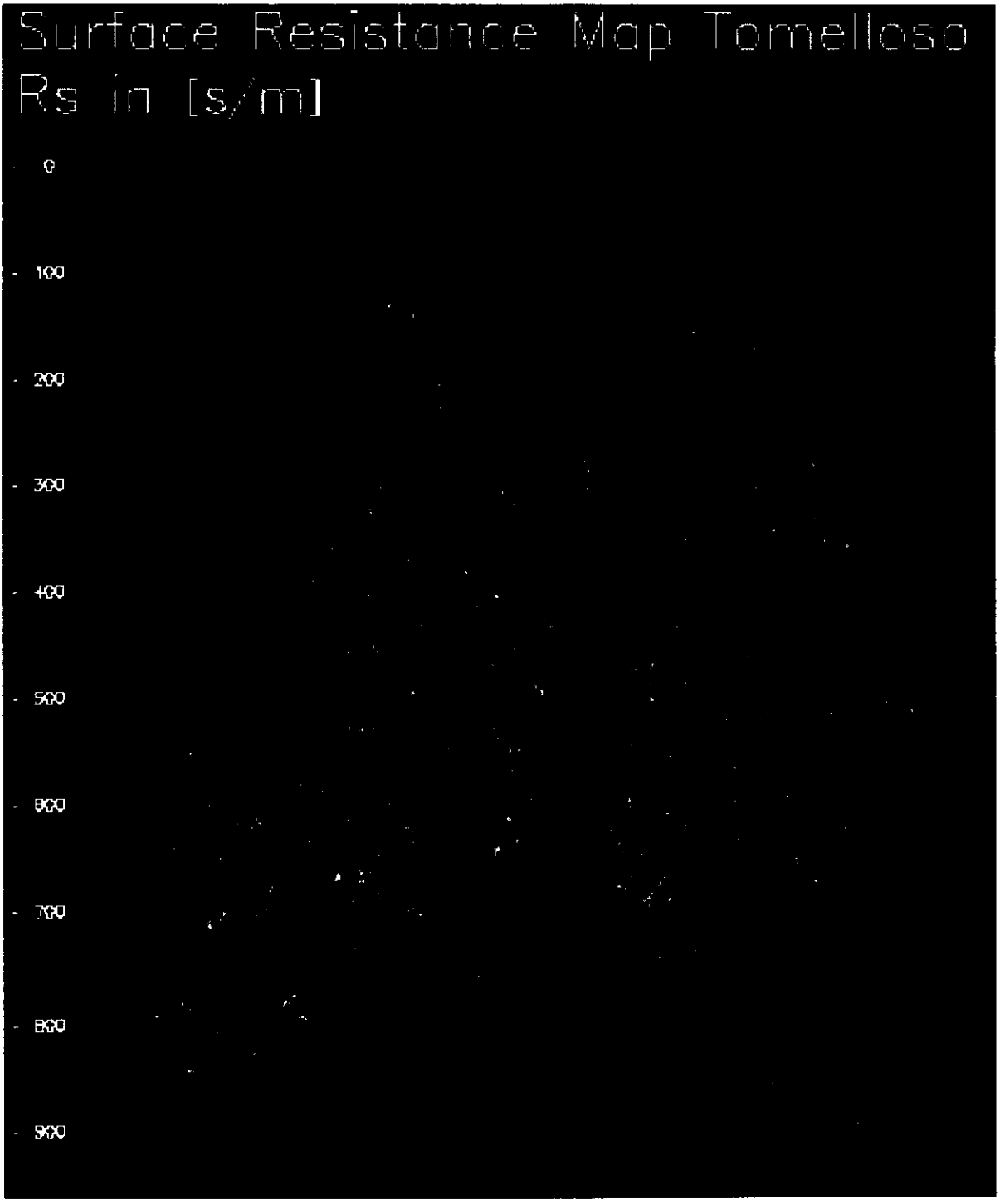
Surface Resistance Map Tomelloso
Rs in [s/m]
0
100
200
300
400
500
600
700
800
900

NAAMSWIJZIGING

Met ingang van 28 januari 1992 is de naam van de vakgroep **Hydrologie, Bodemnatuurkunde en Hydraulica** gewijzigd in **Waterhuishouding.**

Inlichtingen zijn verkrijgbaar bij het secretariaat van de vakgroep:
telefoon : 08370 - 82293/82778
telefax : 08370 - 84885
Vakgroep Waterhuishouding
Landbouwuniversiteit
Nieuwe Kanaal 11
6709 PA Wageningen

For further information please contact the secretariat of the department:
telephone : 31 - 8370 - 82293/82778
telefax : 31 - 8370 - 84885
Department of Water Resources
Agricultural University
Nieuwe Kanaal 11
6709 PA Wageningen
The Netherlands

OVERZICHT VERSCHENEN RAPPORTEN

Nr	Auteur(s) + titel	Prijs (Hfl)
1.	Promes, P.M. 1990. De problematiek van de koppeling van grondwatermodellen en openwatermodellen.	*
2.	Kors, A.G. en P.M. Promes, 1990. Gebruikershandleiding voor het openwatermodel LYMPHA.	*
3.	Dommerholt, A. en P.M.M. Warmerdam (redaktie), 1990. Verslag van de buitenlandse excursie naar Münsterland, het Ruhrgebied en de Eifel. 4 t/m 7 september 1989.	*f* 14,00
4.	Simunek, J. 1990. Analysis of soil survey data of the Hupselse Beek.	*f* 14,00
5.	Dirksen, C. 1990. Unsaturated hydraulic conductivity.	*f* 19,50
6.	Boiten, W. 1990. Afvoerrelatie V-vormige vistrap.	*
7.	Dam, J.C. van, J.N.M. Stricker en P. Droogers, 1990. From one-step to multi-step. Determination of soil hydraulic functions by outflow experiments.	*f* 21,00
8.	Boiten, W. 1990. Advies debietmeetstation Oude Diep te Echten.	*
9.	Promes, P.M. 1990. De koppeling van het grondwatermodel GELDYM-MUST en het openwatermodel LYMPHA. Model TRIGON.	*
10.	Amerongen, F. van, R. Dijksma en J.M. Schouwenaars, 1990. Hydrologisch onderzoek in het hoogveengebied De Engbertsdijksvenen. (Verslag van de belangrijkste resultaten en verzamelde gegevens in de periode 1987-1989).	*f* 24,50
11.	Moene, A.F. 1990. The addition of retention data derived from pedotransfer functions in one-step outflow optimization.	*f* 21,00

* Voor inlichtingen over dit rapport dient u zich te wenden tot de opdrachtgever.

Nr	Auteur(s) + titel	Prijs (Hfl)
12.	Boiten, W., 1991. Afvoeren Nieuwe Ley te Goirle.	*
13.	Schaaf, S. van der en C.J. de Vries, 1991. Integraal waterbeheer Ede. Deelrapport ontwatering.	*
14.	Boiten, W., 1991. Meetadvies afvoerbepaling via twee suatiesluizen.	*
15.	Schaaf, S. van der, 1991. Gevolgen van de aanleg van de rondweg S-25 bij Veenendaal en daarmee verband houdende ingrepen voor de waterhuishouding van Hel en Blauwe Hel.	*
16.	Verhoef, A. en R.A. Feddes, 1991. Preliminary review of revised FAO radiation and temperature methods.	*f* 24,50
17.	Voet, P. van der en J.P.M. Witte, 1991. Redesign DEMGEN: Hydrologische schematisering van PAWN-district 29 (Noordwest Veluwe) met een geografisch informatiesysteem. Een haalbaarheidsonderzoek.	*
18.	Boiten, W., A. Dommerholt en L.J.J. Dijkhuis, 1991. Hydrologisch meetplan waterschap Lits en Lauwers.	*
19.	Bier, G., D. van der Hoek, S. van der Schaaf (red.) en T.J. Spek, 1992. Kwel en natuurontwikkeling in het Binnenveld tussen de Neder-Rijn en Veenendaal. Deel 1: Tekst, Deel 2: Bijlagen.	*f* 50,00
20.	Uijlenhoet, R., 1992. A simple surface radiation budget model for a point in snow covered mountainous terrain.	*f* 31,00
21.	Brorens, B.A.H.V., 1992. Water resource system training model "WATSYS". User's manual.	*f* 21,00
22.	Vries, C.J. de, 1992. Hydrologische gegevensbestanden in de Gelderse Vallei, het Binnenveld en het proefgebied de Veenkampen. Gegevens voor het modelleren van proefgebied de Veenkampen met het niet-stationaire grondwaterstromingsmodel SIMGRO.	*f* 16,50
23.	Vries, C.J. de, 1992. Stedelijk grondwaterbeheer. Het optimaliseren van het grondwater-meetnet van de gemeente Ede.	*
24.	Vermulst, J.A.P.H., 1992. Redesign DEMGEN: Een voorstel tot groepering van grondwatertrappen.	*
25.	Vermulst, J.A.P.H., 1992. Redesign DEMGEN: Toetsing van de hydrologische schematisatie op afvoeren van de Schuitebeek.	*
26.	Stricker, J.N.M. (editor), 1992. Urban/rural application of weather radar for flow forecasting. Proceedings of the informal CEC-workshop in Wageningen, december 1990.	*f* 25,00
27.	Boiten, W., 1992. Northern Tunisia Water Resource Management Project. Report of a preappraisal mission for the World Bank, april 26 - may 4, 1992.	*
28.	Dommerholt, A. en P.M.M. Warmerdam (redaktie), 1992. Verslag van de buitenlandse excursie naar het Ruhrgebied en de Harz. 18 tot en met 22 mei 1992.	*f* -,-
29.	Dommerholt, A., 1992. Afwijkingen in gemeten waterstanden. Waterstandsmetingen met peilbuis en intake pipe.	*f* 13,50
30.	Boiten, W., 1992. Vertical gates for distribution of irrigation water.	*f* 10,00
31.	Vissers, M.A.M. en J.J. van der Sanden, 1992. Groundtruth collection for the JPL-SAR and ERS-1 campaign in Flevoland and the Veluwe (NL) 1991.	*

Nr	Auteur(s) + titel	Prijs (Hfl)
32.	Ignar, S. en J.J. Bogardi, 1993. Rainfall-runoff model for design flood computation with variable parameters.	*f* 10,50
33.	Maren, G. van en C. Varekamp, 1993. Combining optical and microwave remote sensing data of forest vegetation. MAC Europe 1991.	*f* 25,00
34.	Oevelen, P.J. van, D.H. Hoekman en M.A.M. Vissers, 1993. Soil moisture and surface roughness measurements during HAPEX-Sahel 1992. Ground data collection report.	*f* 12,50
35.	Slik, P.C. 1993. Time Domain Reflectometry for measuring bulk soil electrical conductivity and comparison with the EM38 instrument.	*f* 17,50
36.	Stricker, J.N.M., J.C. van Dam en P. Droogers, 1993. Spatial variability of land surface processes under programme: climate. Final report.	*
37.	Droogers, P., G.D. v.d. Abeele, J. Cobbaert, C.P. Kim, R. Rösslerová, M. Soet en J.N.M. Stricker, 1993. Basic data sets description and preliminary results of EFEDA-Spain.	*f* 24,50
38.	Bastiaanssen, W.G.M., D.H. Hoekman en R.A. Roebeling, 1993. A methodology for the assessment of surface resistance and soil water storage variability at mesoscale based on remote sensing measurements. A case study with HAPEX-EFEDA data.	*f* 33,00